Progress In Electromagnetics Research, PIER 39, 299–339, 2003

FINITE DIFFERENCE TIME DOMAIN MODELING OF LIGHT AMPLIFICATION IN ACTIVE PHOTONIC BAND GAP STRUCTURES

A. D'Orazio, V. De Palo, M. De Sario, V. Petruzzelli and F. Prudenzano

Dipartimento di Elettrotecnica ed Elettronica
Politecnico di Bari
Via Re David, 200-70125 Bari, Italy

Abstract—The paper deals with the modeling, based on the Finite Difference Time Domain method, of active one- and two-dimensional photonic crystals. The onset of laser oscillation is observed by simulating the active substance as having a negative frequency-dependent Lorentzian-shaped conductivity so including into Maxwell's equations an electric current density. Particular attention is devoted to the implementation of uniaxial perfectly matched layer absorbing boundary conditions for the simulation of infinitely extending structures having gain features. Laser behaviour is simulated as a function of various parameters; the threshold wavelength and conductivity are evaluated as the wavelength and conductivity where the transmittance diverges. Moreover, the properties of the active two-dimensional photonic band gap structures are given in terms of a Q quality factor which increases by increasing the crystal size and strongly depends on the lattice shape. For the square lattice, when the crystal size increases from $N = 2$ to $N = 8$ the Q-factor increases by about an order of magnitude (from 0.027 to 0.110) for TE polarization while for TM polarization it decreases from 0.025 to 0.022. At last the Q-factor pertaining to the chess-board lattice, to parity of other parameters, assumes greater values and already for $N = 4$, it reaches the values obtained for the 16×8 square lattice, for both TE and TM polarizations.

1 Introduction

2 FDTD Modeling of PBG Structures with Lorentzian Gain Media

3 1D PBG Structure Simulation Results

4 2D PBG Structure Numerical Results

5 Conclusion

Appendix A. 2D FDTD Algorithm for Active Materials

Appendix B. PML Termination for Conductive Dispersive Media

References

1. INTRODUCTION

Electromagnetism is the fundamental mediator of all interactions in atomic physics and condensed matter physics, in other words, the force that governs the structure of ordinary matter. In a novel class of engineered dielectric materials, known as photonic crystals (PhCs) or Photonic Band Gap (PBG) materials, new electromagnetic effects can be obtained [1–4]. The light localization is a particular interesting phenomenon of fundamental importance for using optical waves in information and communication technologies. Because of the periodic spatial modulation of the dielectric constant, the dispersion equation of the electromagnetic eigenmodes in photonic crystals are quite different from those in uniform materials. A part from the formation of pass bands and band gaps of eigenfrequencies, extremely small group velocity (the derivative of the angular frequency ω of the radiation field with respect to the wave vector $\boldsymbol{k}, \boldsymbol{v}_g = d\omega/d\boldsymbol{k}$) can be easily obtained in a photonic crystal. In fact a large enhancement of light amplification is obtained when v_g is small, the amplitude amplification factor being proportional to v_g^{-1} [5].

By considering the photonic band structure, given by the normalized frequency $\omega_n = \omega a/2\pi c$ as a function of the wave vector $\boldsymbol{k}$ (a and c being the lattice constant and the light velocity in the vacuo, respectively) of a one-dimensional (1D), or two-dimensional (2D) or three-dimensional (3D) lattice, it is possible to find that there exist points, exactly the band gap edges, where v_g is equal to zero. Moreover, the photonic band structure of a 2D or a 3D PhC shows whole frequency ranges in the Brillouin zone characterized by a small group velocity. This phenomenon, known as the group velocity anomaly,

is peculiar to 2D and 3D photonic crystals and it does not occur in 1D periodic structures. The enhancement of light amplification due to a small group velocity can be so explained [6]: since the photon undergoes many multiple reflections at the lattice discontinuities, the optical path length increases and the photon spends a long time in the lattice moving at a mean velocity equal to v_g. In presence of an active medium, the increase of the interaction time between radiation field and matter gives rise to the enhancement of gain.

A subsequent effect of these phenomena is the laser oscillation onset which can be obtained in any type of PhC, not depending on the geometrical complexity of the lattice. In particular, Ohtaka [7] verified that the onset of the laser oscillation is due to the presence of divergent peaks in the transmission spectrum. In the case of 1D PhCs, this phenomenon occurs when high gain materials and an opportune number N of lattice periods are involved, while lower N (even $N = 1$) and drastically reduced threshold gain values are required in 2D and 3D PhCs in order to obtain the same laser action. On the other hand, it was shown that the 1D PBG lattices exhibit nearly the same lasing properties aside from the band location in the frequency spectrum. This is in clear contrast to the lasing action in 2D or 3D photonic crystals, where the onset of the lasing in higher bands is much easier than in the first band.

A number of prototypal "active" devices based on photonic crystals were designed, constructed and tested [8–16]. As an example, Inoue et al. [17] reported the observation of lasing action in a 2D photonic lattice. By optically pumping a dye-solution filled in air-holes of the 2D lattice, laser action without external mirrors is found to occur at a specific wavelength corresponding to a flat band-dispersion in high-symmetry direction of the 2D lattice plane, the small group velocity being responsible for the lasing. Further increasing the pump-fluence, another laser action is found to occur around a peak wavelength of the spontaneous emission spectrum.

Moreover, strong feedback and memory effects accompany collective light emission near the photonic band edge. Near a true 3D photonic band edge, this leads to lasing without a conventional optical cavity. A precursor of this effect was found in the 2D band edge micro-laser [18] in which lasing from electrically injected electron-hole pairs in a multiple quantum well array occurs preferentially at the 2D photonic band edge, even though the emission from the active region exhibits a broad frequency distribution.

The active PhC technology offers significant promises in this arena but, before this can become a true reality, a number of technological barriers, as repeatable and high-fidelity technologic processes,

high efficiency input and output-coupling devices, manufacturing integration methods, and so on must to be overcome. Apparently, the engineering perspective of PhC devices requires development of reliable design tools. As it is well known, the first theories of PhCs were based on the solid-state physics and band-theory for semiconductor materials. Due to the vector nature of electromagnetic (e.m.) fields, these early analyses proved their inaccuracy so mathematical tools, incorporating the vector nature of e.m. fields, have been developed. A largely used technique, which gives results with good agreement with the experimental ones, is the Plane Wave Method (PWM) where an infinite period lattice is assumed. This method is no longer valid when a linear defect or a point defect is included in the lattice or when a finite period lattice is considered. For this reason, alternative tools have been developed: one of the more common is the finite-difference time-domain (FDTD) method [19].

Till now, active PhC device modeling has been performed in the frequency domain by assuming the polarizability of the impurity atoms of the gain material independent of angular frequency ω and the impurities uniformly distributed in the dielectric material: in this case the gain material can be modeled by simply assuming a complex dielectric constant (with a negative imaginary part which incorporates the population inversion phenomena, the field time dependence being $\exp(-j\omega t)$. As an example, this formalism was used in [7] to describe the light amplification in active two-dimensional photonic crystals. In this paper, we describe a FDTD formulation that allows the modelling of PBG structures having frequency-dependent optical gain media. The frequency dependent gain is incorporated into the electric current density term in Maxwell's equations by means of a Lorentzian frequency-dependent negative conductivity. To our knowledge, this is the first study performed on active PhC devices by means of FDTD.

The paper is organized as it follows. Sect. 2 briefly resumes the principles of the FDTD method, referring the Reader to the Appendices A and B for more deepening. In particular, Appendix A describes the fundamentals of FDTD operation in the case of 2D photonic crystals when the frequency dependent gain is incorporated into the electric current density term in Maxwell's equations; Appendix B models the uniaxial perfectly matched layer (UPML) absorbing boundary conditions in presence of infinitely extending active media. The reduction of the developed equations for the 1D periodic structures can be easily obtained from those obtained for 2D ones while the extension to the 3D periodic structures requires a light, even if tedious, algebraic loading. Sect. 3 of the paper reports the results of the simulations performed on active 1D photonic crystals.

In particular, the light amplification spectra are numerically evaluated and the lasing threshold conditions are identified by examining the divergence of transmission and reflection coefficients. Lastly, in Section 4 we discuss the strength of the FDTD-based numerical code devoted to the analysis of active 2D photonic crystals. In particular, the effect of the lattice shape on the amplification and transmission characteristics is evaluated.

2. FDTD MODELING OF PBG STRUCTURES WITH LORENTZIAN GAIN MEDIA

In this section we briefly describe the home-made FDTD algorithm that allows us the modeling of the active PBG structures. The process of light emission in active PhCs is analogous to the lasing oscillation in distributed feedback lasers: the onset of lasing is equivalent to the divergence of the transmittance and/or the reflectance of the assumed specimen, as demonstrated by Yariv [20]. Because we are interested in the evaluation of the lasing threshold conditions, we will disregard in what follows the nature of the active substance and we will simply assume that the optical impurities (atoms or molecules) are uniformly distributed in the photonic crystal and their population inversion is attained by appropriate means such as optical pumping. Under these same hypothesis, several authors [7, 21] modeled the active substance in the frequency domain by a complex frequency-independent dielectric constant with a negative imaginary part. In our analysis developed in the time domain, we consider active structures composed by frequency-dependent optical gain media. The frequency dependent gain is incorporated into the electric current density term in Maxwell's equations by means of a Lorentzian frequency-dependent negative isotropic conductivity given by:

$$\begin{aligned}\sigma(\omega) &= \frac{J_x(\omega)}{E_x(\omega)} = \frac{J_y(\omega)}{E_y(\omega)} = \frac{J_z(\omega)}{E_z(\omega)} \\ &= \frac{1}{1+I/I_s}\left(\frac{\sigma_0/2}{1+j(\omega-\omega_0)T_2} + \frac{\sigma_0/2}{1+j(\omega+\omega_0)T_2}\right) \qquad (1)\end{aligned}$$

where σ_0 is the conductivity peak value, linked to the peak value of the gain set by the pumping level and the corresponding population inversion; ω_0 is the frequency pertaining to the peak value of the conductivity; T_2 is a time constant that defines the spreading of the Lorentzian spectral profile, $S = (1+I/I_s)^{-1}$ is the saturation coefficient while I_s is the saturation intensity. In Eq. (1), the Hermitian symmetry is used for the Lorentzian profile.

The idea of using negative conductivity to describe gain media has been inspired by the work in the microwave community where positive conductivity is used to simulate the lossy media. So, if positive conductivity can be used to simulate the attenuation aspects of a dispersive medium, then a negative conductivity might be useful for simulating a medium with gain. The choice of Lorentzian shape for the conductivity is based on the consideration that more complicated and, overall, experimental gain spectra can be approximated using a linear combination of Lorentzians. Another assumption is implicit in disregarding the nature of the active substance: no interaction between the input signal and other fields (such as the optical pump) is considered.

The FDTD method is formulated using a central difference discretization of Maxwell's curl equations in both time and space (see Appendix A). Yee's original algorithm and formalism solving Maxwell's equations in two dimensions is adopted. The field values on the nodal points of the discretized finite volume are calculated in a leapfrog fashion. Due to the use of centered differences in the approximations, the error is of second order in both the space $(\Delta x, \Delta z)$ and time (Δt) steps. In the calculations, the maximum time step that may be used is limited by the stability restriction of the finite difference equations.

The excitation plane needs to be treated carefully when setting up the problem. If a Gaussian source is used as the excitation source, its smooth Gaussian shaped spectrum can provide information from dc to the desired frequency simply by adjusting the width of the pulse. Therefore, in the following simulations a Gaussian pulse PG is assigned to specific electric or magnetic field components in the FDTD space lattice at the grid source point (i_S, j_S, k_S):

$$P_G = \exp(-(n - n_o)/n_d)^2 \tag{2}$$

This pulse is centered at time step n_o, exhibits a $1/e$ characteristic decay of n_d time steps and it has a nonzero value at $n = 0$.

The successful implementation of the FDTD algorithm is conditioned by the inclusion of accurate and efficient absorbing boundary conditions to emulate electromagnetic interaction in an unbounded space. The perfectly matched layer (PML) absorbing medium is the ideal candidate for the grid termination, but its definition have to be modified when the computational volume is totally filled with active medium (see Appendix B). In particular, in the developed code, the UPML are adopted: the conductivity profile for each side $(i = x, y, z)$ of the grid is defined as:

$$\sigma^{PML}(i) = \sigma_m g^{N_{PML}} \tag{3}$$

with

$$\sigma_m = [\ln R(0) \ln g)/(2\eta\varepsilon\Delta i(g^{N_{PML}} - 1)]$$

where η is the vacuum characteristic impedance, N_{PML} is the cell number which gives the UPML thickness, g is the geometric scaling of PML conductivity profile, $R(0)$ is the reflection error for normal incidence and Δi is the spatial step size.

FDTD algorithm allows for obtaining the reflection and transmission coefficients over a wide band of frequencies in one run. In our analysis the electromagnetic performance of the PBG structure is described by means of transmission (transmittance T) and reflection (reflectance R) coefficients, defined in terms of the total time-averaged Poynting's vector through the input ($z = 0$) and output ($z = L$) sections:

$$\begin{aligned} T &= \frac{P_t(z=L)}{P_i(z=0)} \\ R &= \frac{P_r(z=\phi)}{P_i(z=0)} \end{aligned}$$

where

$$\begin{aligned} P_i &= -\frac{1}{2}\mathrm{Re}\left[\int_{width} E_{i_{i,\omega}}(x, z=0) H^*_{i_{i,\omega}}(x, z=0) dx\right] \\ P_r &= -\frac{1}{2}\mathrm{Re}\left[\int_{width} E_{r_{i,\omega}}(x, z=0) H^*_{r_{j,\omega}}(x, z=0) dx\right] \\ P_t &= -\frac{1}{2}\mathrm{Re}\left[\int_{width} E_{t_{i,\omega}}(x, z=L) H^*_{t_{j,\omega}}(x, z=L) dx\right] \end{aligned}$$

and $E_{i_{i,\omega}}$ and $H_{i_{j,\omega}}$ represent, in the frequency domain, the incident electric and magnetic field components, obtained numerically anti-transforming Eqs. (A3) and (A4) of Appendix A. Moreover the subscripts i and j indicate the components $E_{i_{y,\omega}}$ and $H_{i_{x,\omega}}$ ($E_{i_{x,\omega}}$ and $H_{i_{y,\omega}}$) for TE (TM) polarization. The symbol (*) indicates the complex conjugate while the integral is extended to the transversal width of the PBG structure along the x direction. The same symbolism is valid for the reflected and transmitted powers, respectively.

3. 1D PBG STRUCTURE SIMULATION RESULTS

The 1D PBG structure under investigation is shown in Fig. 1. It is composed of N layers of active material in air ($\varepsilon_1 = 1$); the dielectric

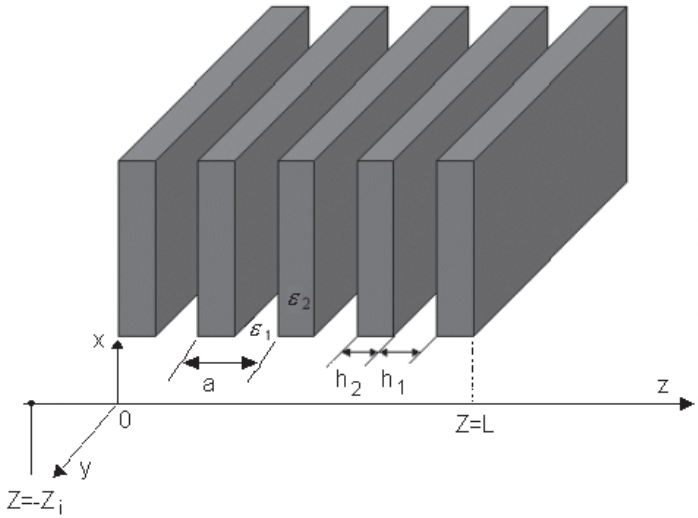

Figure 1. Sketch of one-dimensional PBG stack structure.

constant ε_2 of the active layers is assumed equal to 2.0 throughout the paper, this value being typical for transparent organic polymers. The lattice constant $a = h_1 + h_2$ is put equal to 1μm, and the thickness h_2 of the active thin layer, normalized by a, is taken to be 0.28. The frequency ω of light, normalized by $2\pi c/a$, is swept in the frequency range of $0 < \omega_n < 2.0$, c being the light velocity in the vacuo. In order to compare our results with those obtained by other methods [7], the central frequency of the examined range corresponds to a frequency $f = 300\,\text{THz}$. We take the xy plane parallel to the layer plane and the z direction in the stack direction.

The FDTD simulations are performed by exciting the PBG structure with a single-cycle Gaussian pulse centered at time step $n_o = 100$, having $n_d = 30$: for these values the pulse bandwidth covers the frequency region of interest. The incident field is evaluated in time domain at the total field/scattered field interface, placed in $z = 0$. The source plane ($z = -z_i$) is located to a distance from this discontinuity equal to $140\,\Delta z$, that allows the complete evolution and the return to zero of the Gaussian pulse, before the reflected wave from the first layer comes back to the source. The reflected field is evaluated in time domain near the section $z = 0$ in the scattered field region; the transmitted field is calculated in time at the point $z = L$, just beyond the end of the PBG structure. The resulting fields are FFT transformed to obtain the frequency spectra.

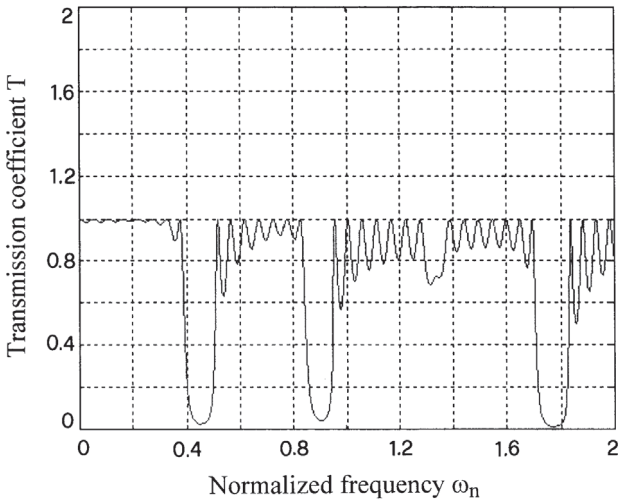

Figure 2. Transmission coefficient T evaluated by means of the FDTD-based code, for the passive PBG structure constituted by $N = 8$ periods of dielectric medium ($\varepsilon_2 = 2.0$) and air; lattice constant $a = 1\,\mu$m; thickness of the dielectric thin films h_2, normalized by a, equal to 0.28.

The UPML conductivity profile for each side ($i = x, y, z$) of the grid is characterized by the following parameters: thickness equal to $N_{PML} = 10$ cells, geometric scaling of PML conductivity profile $g = 2.5$, reflection error for normal incidence $R(0) = \exp(-16)$ and Δi equal to the spatial step size. The FDTD computational window is identified by a lattice pitch $\Delta z = \lambda/500 = 2\,\text{nm}$ in space with $\lambda = 1\,\mu$m corresponding to the central frequency of the examined range, and $\Delta t = \Delta z/c = 6.66\ 10^{-3}\,\text{fs}$. These values of the computational domain steps guarantee good numerical dispersion and stability [4].

We start our simulations by analyzing the periodic passive stack constituted by $N = 8$ periods of dielectric layers having $\varepsilon_2 = 2.0$ and $\varepsilon_1 = 1$ (air). Fig. 2 shows the evaluated transmission coefficient of the $N = 8$ period passive stack. The transmission spectrum shows four band gaps, three of them well defined and centered at the ω_n normalized frequency values equal to 0.44, 0.9 and 1.76 respectively, while the band gap centered at $\omega_n = 1.35$ is just hinted reaching only the value of $T = 0.7$. These results are in good agreement with those calculated by using a computer code based on the transfer-

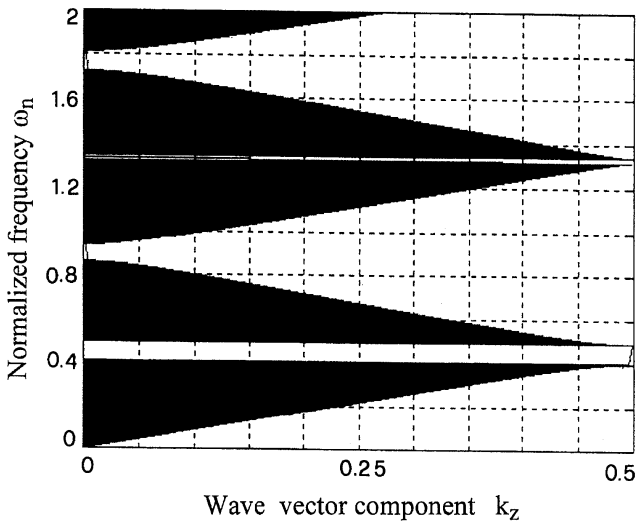

Figure 3. Band structure, obtained by a TMM-based code, of the infinite PBG stack lattice of dielectric material in air. Other data as those in Fig. 2.

matrix (TMM) approach [22]†. In particular, Fig. 3 shows the band structure, evaluated by TMM, for the wave vector $(0, 0, k_z)$ of the x, y axis infinite periodic stack, by disregarding the active nature of the dielectric substance (k_z, of course, is the wave vector component in the stack direction). In the analyzed range of normalized frequency, we notice four band gaps, the not shaded spectral ranges representing the band gaps. The first band gap is located in the range of normalized frequency $0.4 < \omega_n < 0.5$, while the following band gaps are in the ranges $0.86 < \omega_n < 0.96$; $1.34 < \omega_n < 1.36$ and $1.72 < \omega_n < 1.80$, for k_z ranging from 0 to 0.5.

Now we consider the active nature of the PBG structure by modeling the active medium 2 by means of a frequency-dependent negative conductivity having a Lorentzian gain profile. Moreover, throughout the paper, we will disregard the saturation effects because the number of time steps does not allow the structure saturation. Our analysis starts by considering a Lorentzian material with an increasing spectral gain profile, characterized by the following parameters: normalized frequency $\omega_n = 2$ (corresponding to a wavelength $\lambda_0 = 0.5\,\mu$m), $\sigma_0 = -3337\,$S/m, $T_2 = 0.7\,$fs. Fig. 4 shows the corresponding

† The program "Translight" can be downloaded from *http://www.elec.gla.uk/~areynolds/software.html*. It is based on the paper by Bell et al. [22]

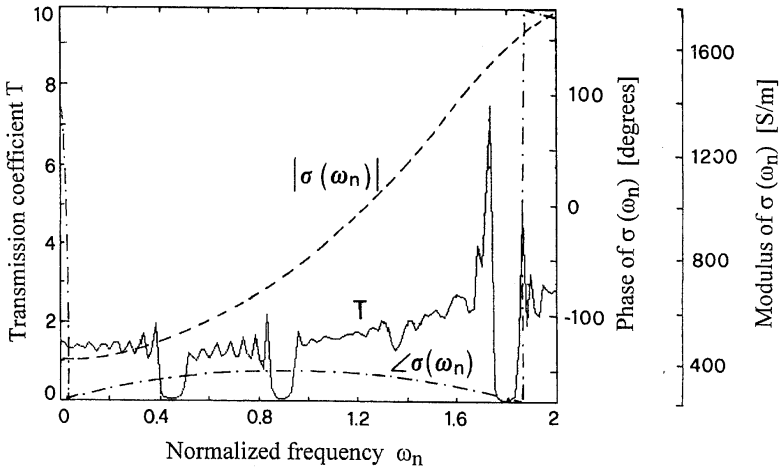

Figure 4. Transmission coefficient of the $N = 8$ period active stack; active Lorentzian material characterized by a conductivity $\sigma(\omega)$ having the following parameters: $\omega_n = 2$ ($\lambda_0 = 0.5\,\mu$m), $\sigma_0 = -3337\,$S/m, $T_2 = 0.7\,$fs, the modulus and phase of $\sigma(\omega)$ are here reported, too. Other data as those in Fig. 2.

modulus (dashed line) and phase (dashed-dotted line) of the above defined conductivity $\sigma(\omega_n)$ and the evaluated transmission coefficient T, obtained by our FDTD-based code, for the PBG active stack constituted by $N = 8$ layers of active material. The transmission coefficient, of course, is higher than that shown in Fig. 2 for the passive PBG structure: the T peak values increase by increasing the frequency, according to the shape of the conductivity modulus, reaching the maximum value $T = 7.5$ in correspondence of the fourth band gap. Moreover, the T peaks are localized at the inferior edge of the band gaps. This is due to the fact that the dielectric constant ε_2 of the gain layer is greater than that ε_1 of the passive layer; while if we assume $\varepsilon_2 < \varepsilon_1$, then we calculate that the maximum T peak values occur at the superior edge of the photonic band gaps, to a parity of other parameters.

Now a Lorentzian material with a decreasing spectral gain profile, characterized by the following parameters: normalized frequency $\omega_n = 1$ (corresponding to $\lambda_0 = 1\,\mu$m), $\sigma_0 = -1668\,$S/m, $T_2 = 0.07\,$fs, is investigated. Even in this example, the evaluated transmission coefficient for the $N = 8$ period active stack, depicted in Fig. 5, shows, also now, peaks localized at the inferior edge of each band gap but they exhibit decreasing values by increasing the frequency. For a greater

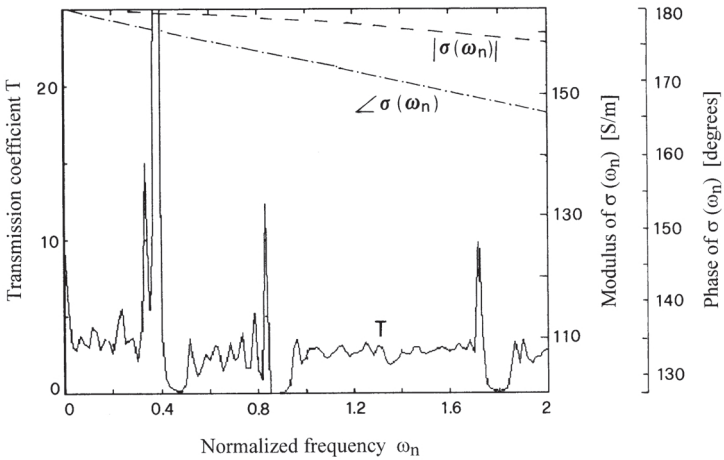

Figure 5. Transmission coefficient of the $N = 8$ period PBG structure having the active Lorentzian material characterized by a conductivity $\sigma(\omega)$ with the following parameters: $\omega_n = 1$ ($\lambda_0 = 1\,\mu$m), $\sigma_0 = -1668\,$S/m, $T_2 = 0.07\,$fs.

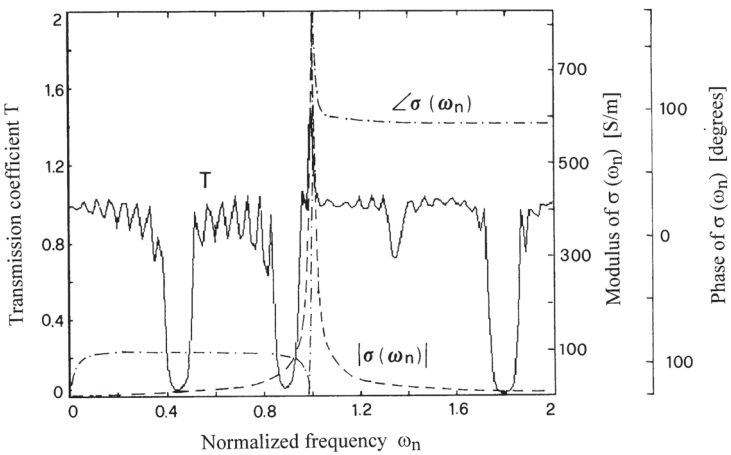

Figure 6. Transmission coefficient of the $N = 8$ period active stack, the active Lorentzian material being characterized by the conductivity $\sigma(\omega)$ having the same numerical values as in Fig. 5 but a greater time constant $T_2 = 0.07\,$ps (narrower frequency range).

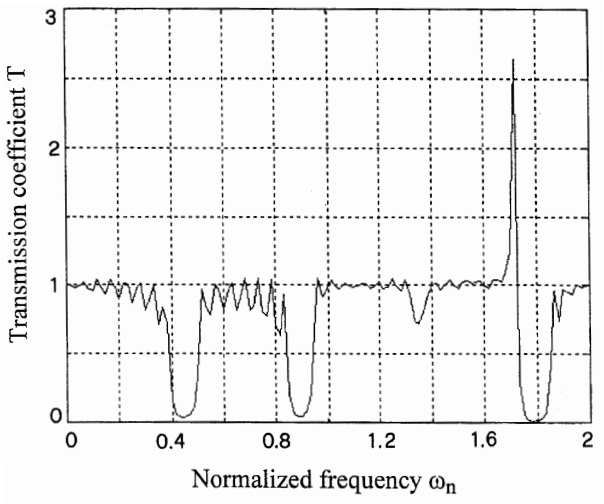

Figure 7. Transmission coefficient of the $N = 8$ period active stack having the active Lorentzian material characterized by the following parameters: $\omega_n = 1.71$ ($\lambda_0 = 0.58\,\mu$m), $\sigma = -2853\,$S/m, $T_2 = 0.07\,$ps; i.e., centered at the inferior edge of the fourth band gap.

time constant T_2, the Lorentzian spectral gain profile is concentrated in a narrow frequency range so, as we can infer from Fig. 6 ($\omega_n = 1$, $\sigma_0 = -1668\,$S/m, $T_2 = 0.07\,$ps), the corresponding transmission spectrum shows a peak value well localized at the frequency value $\omega_n = 1$ which corresponds to the maximum value of the conductivity and, of course, it is characterized by the same T values pertaining to the passive stack out of the very narrow frequency range centered at $\omega_n = 1$.

A sensible enhancement of the peak value of the transmission coefficient T is obtained by fixing the frequency of maximum conductivity just in correspondence of an edge frequency of a band gap. As an example, by considering the Lorentzian conductivity profile ($\sigma_0 = -2853\,$S/m, $T_2 = 0.07\,$ps) having the maximum value fixed at the inferior edge of the fourth band gap $\omega_n = 1.71$ ($\lambda_0 = 0.58\,\mu$m), we obtain the transmission coefficient plot shown in Fig. 7 which exhibits a good peak just at $\omega_n = 1.71$. Of course, if we center the Lorentzian at the superior edge $\omega_n = 1.86$ ($\lambda_0 = 0.53\mu$m) of the same fourth band gap, we obtain the spectrum of Fig. 8 where the peak at $\omega_n = 1.86$ is apparent.

By comparing these spectra, we infer that the shift of the conductivity peak value into correspondence of an edge of a band gap induces a sensible enhancement of the peak value of the transmission

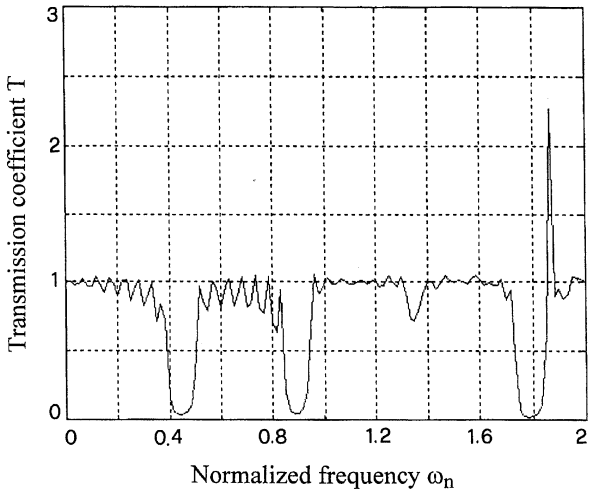

Figure 8. Transmission coefficient of the $N = 8$ period active stack having the active Lorentzian material characterized by the following parameters: $\omega_n = 1.86$ ($\lambda_0 = 0.53\,\mu$m), $\sigma = -2853\,$S/m, $T_2 = 0.07\,$ps; i.e., centered at the superior edge of the fourth band gap.

coefficient. Moreover by choosing the frequency of the conductivity peak at the superior edge of the photonic band gap (Fig. 8), the transmission coefficient reaches a peak value slightly smaller than obtained when the conductivity peak is located at the inferior edge (Fig. 7). By resuming, the best value for the transmission coefficient is obtained choosing the frequency of maximum conductivity in correspondence of the inferior edge of the band gaps. Moreover, we have verified that, to parity of N, the photonic band structure of 1D periodic stack shows nearly the same amplification properties irrespective of the band position in frequency. These results are in good agreement with those published in literature.

So far we have examined the dependence of the transmission spectra on the Lorentzian conductivity shape. Now we will illustrate the effects of the increase of the period number N. Our starting point is the optimum transmission spectrum obtained for the $N = 8$ period active stack, shown in Fig. 7 pertaining to the active medium having the Lorentzian conductivity peak centered at the inferior edge of the fourth band gap. By considering an active stack having $N = 16$ periods, the transmission peak increases from 2.6 (see Fig. 7) to 9, as shown in Fig. 9. The effect is more evident if the number of active layers is increased to $N = 32$ (see Fig. 10): the transmittance peak

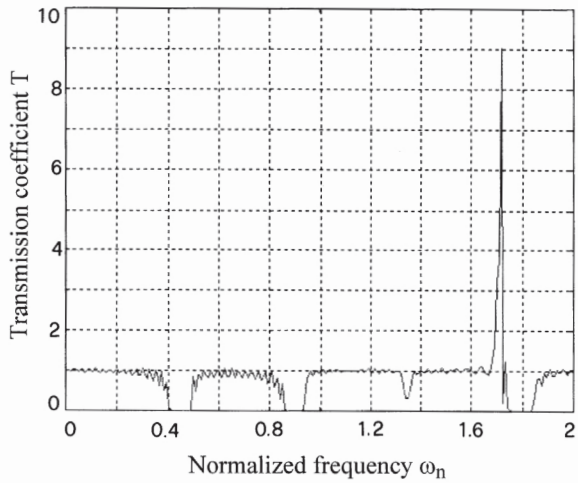

Figure 9. Transmission coefficient of the $N = 16$ period active stack; other data as those in Fig. 7.

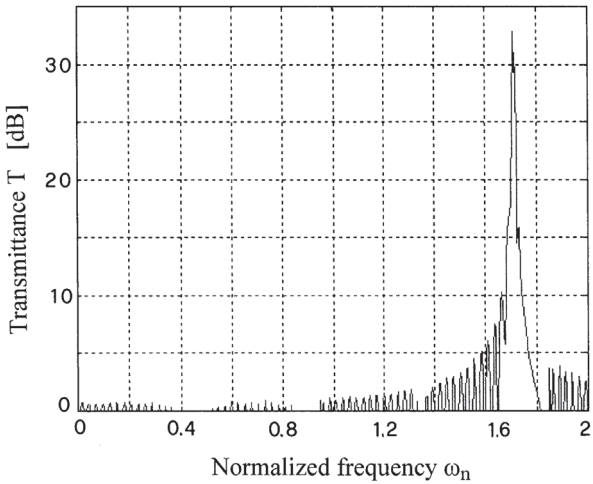

Figure 10. Transmittance of the $N = 32$ period active PBG structure having an active Lorentzian material characterized by the following parameters: $\omega_n = 1.71$, $\sigma_0 = -2853\,\mathrm{S/m}$, $T_2 = 0.07\,\mathrm{ps}$.

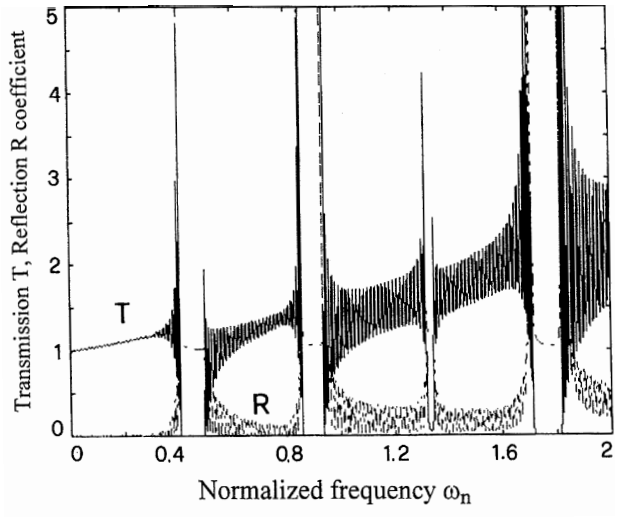

Figure 11. Transmission and reflection coefficients of the $N = 32$ period active stack, obtained by the TMM-based code, by modeling the active layer by a the complex dielectric constant $\varepsilon = 2.0 - j0.01$.

reaches about 34 dB. The divergence of the T coefficient is indicative of the onset of the laser oscillation as we will see in Fig. 13. On the other hands, the stack having $N = 8$ periods is characterized by a threshold conductivity value, which gives rise to a T singularity equal to about 32 dB, $\sigma_0 = -19971\,\mathrm{S/m}$, value seven times greater than that considered for the 32-period active stack ($\sigma_0 = -2853\,\mathrm{S/m}$).

To definitively validate the effectiveness of the developed FDTD-based code, the same structure has been simulated by the TMM-based code. Acting the TMM in the frequency domain, the properties of the active material have been incorporated into the negative imaginary part ε'' of the dielectric constant of the active layers $\varepsilon_2 = \varepsilon' + j\varepsilon''$, with $\varepsilon' = 2.0$. The population inversion has been taken into account into the negative imaginary part ε''. The results obtained for the case $N = 32$ period active stack layers with $\varepsilon_2 = 2.0 - j0.01$ (time operator $e^{-j\omega t}$), are shown in Fig. 11.

In the FDTD algorithm, we have then introduced the electric current density expressed by means of an equivalent negative conductivity given by $\sigma_{eq} = \omega\varepsilon_0\varepsilon''$. Of course this model is exact only at the frequency that defines the equivalent conductivity; for this reason the analysis is applied to the third band gap that is narrower than the others. The transmission and reflection coefficients for a stack consisting of $N = 32$ layers of active material having $\sigma_{eq} = 223.4\,\mathrm{S/m}$

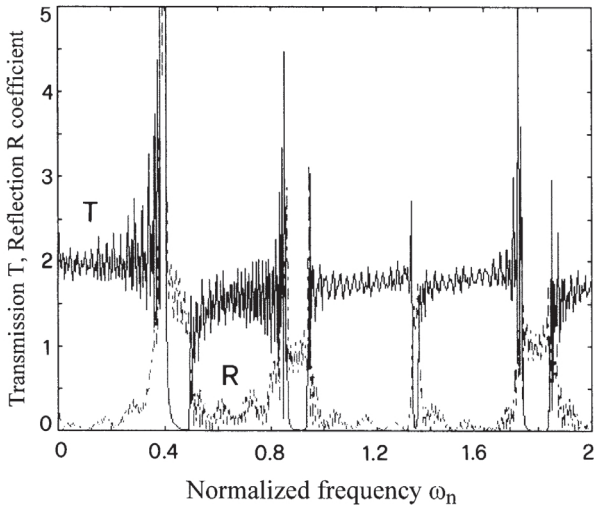

Figure 12. Transmission and reflection coefficients of the $N = 32$ period active stack, obtained by the FDTD-based code by assuming in Maxwell's propagator an equivalent conductivity $\sigma_{eq} = \omega\varepsilon_0\varepsilon'' = 223.4\,\mathrm{S/m}$, $\omega_n = 1.34$.

at the normalized frequency $\omega_n = 1.34$, corresponding to $\varepsilon'' = 0.01$ are shown in Fig. 12. At the normalized frequency value $\omega_n = 1.34$, where the σ_{eq} has been evaluated, the results obtained by means of both methods are in good agreement, within the bounds of the different computation resolution. In fact the FDTD code accounts 480 samples in the examined range of normalized frequency while the TMM simulation accounts 9999 samples in the same normalized frequency range.

The lasing oscillation, observed by the FDTD simulator, is depicted in Fig. 13 which shows the evaluated time evolution of the electric field E_y in the output section of the 32-period Lorentzian ($\lambda_0 = 0.58\,\mu\mathrm{m}$, $\sigma_0 = -2853\,\mathrm{S/m}$, $T_2 = 0.07\,\mathrm{ps}$) active stack. For these data, the T coefficient exhibits a divergent peak at the lower edge of the fourth band gap and all the electric and magnetic field component amplitudes, but overall the E_y component, increase in time. The field component E_y tends to level off to a sinusoidal steady-state oscillation at the frequency that defines the maximum of the conductivity. This is apparent in Fig. 13 where the final time steps are plotted in expanded time scale.

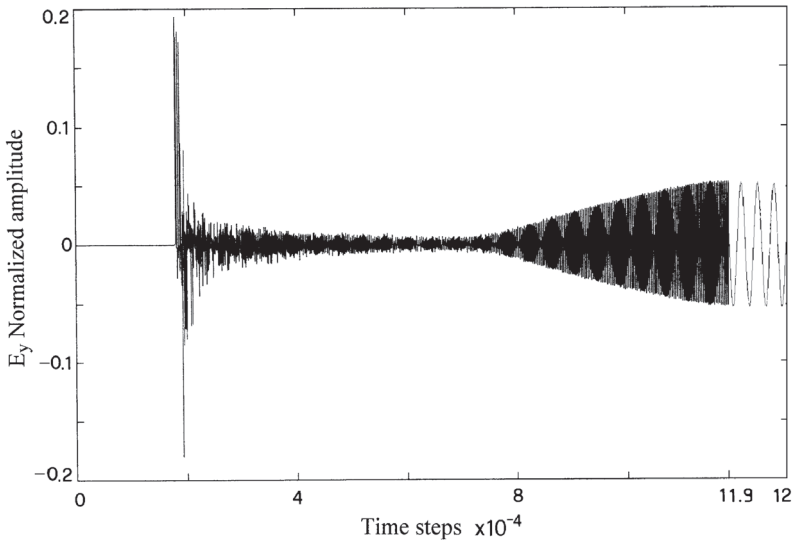

Figure 13. FDTD-computed time evolution of the electric field component E_y in the output section for the case $N = 32$, $\omega_n = 1.71$ ($\lambda_0 = 0.58\,\mu$m), $\sigma_0 = -2853\,$S/m, $T_2 = 0.07\,$ps.

4. 2D PBG STRUCTURE NUMERICAL RESULTS

The 2D PBG structure, under investigation, consists of M columns of active material in air, located along the x direction and N columns along the propagation direction z, the infinitely long column axis lying along the y-axis. The relative dielectric constant ε_2 of the active layers is assumed equal to 2.0 throughout the paper. The columns have a square cross-section and are arranged in a square lattice (see Fig. 14a) having lattice constant a, equal to $1\,\mu$m. The square column side d, normalized by a, is taken equal to 0.53. The light normalized frequency ω_n is assumed in the frequency range of $0 < \omega_n < 2.0$.

The band structures for the corresponding $M = N = \infty$ passive 2D photonic crystal, evaluated for TE and TM polarizations, show total band gaps in the ranges of normalized frequency $0.44 < \omega_n < 0.56$ and $0.82 < \omega_n < 0.9$, for the wave vector component k_z ranging from 0 to 0.5. For the considered lattice, the TE polarization accounts for the E_y, H_x and H_z field components, while the TM polarization is characterized by the H_y, E_x and E_z field components.

To evaluate the spectral characteristics of the 2D PBG structures, the proprietary FDTD simulator has been used under the following

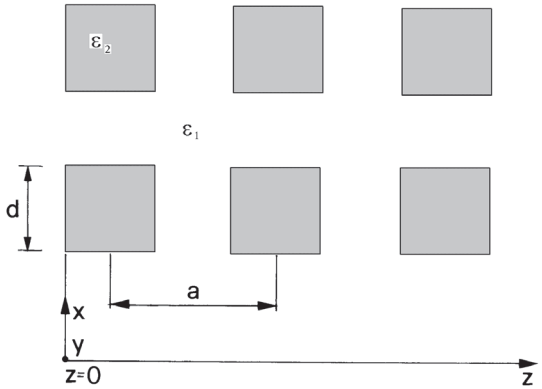

(a)

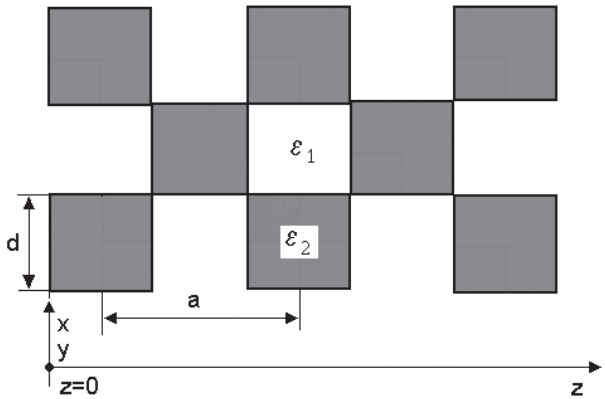

(b)

Figure 14. Cross section of the elementary cell of a two-dimensional PBG structure characterized by: (a) a square lattice and (b) a chessboard lattice.

conditions. The 2D PBG structure is excited with a single-cycle Gaussian pulse ($n_o = 50$, $n_d = 5$), located to a distance from the first discontinuity equal to $z_i = a/2 = 500\,\text{nm}$. The FDTD grid accounts space steps equal to $\Delta x = \Delta z = \lambda c/25 = 40\,\text{nm}$, and time step $\Delta t = \Delta z/(c \cdot \sqrt{2}) = 9.42\ 10^{-2}\,\text{fs}$. The UPML parameter values are the same assumed in Sect. 3.

The first aim of this investigation consists of illustrating the

influence of a finite number of periods N along the z direction on the spectral characteristics, having fixed $M = 16$ columns along the x axis. For this reason, a square lattice of $M \times N = 16 \times 2$ columns of dielectric passive material ($\varepsilon_2 = 2.0$) in air is at first considered. Fig. 15 shows the FDTD evaluated transmission T and reflection R coefficients for: (a) TE and (b) TM polarizations. These results resemble the ones evaluated for the infinite passive square lattice; in fact a well defined photonic band gap is observable for a normalized frequency of $\omega_n = 0.9$ in the case of TE polarization while the transmission dip of TM polarization reaches only the value of 0.5. Moreover the first band gap near the normalized frequency $\omega_n = 0.4$, visible in the band structure of the infinite passive PBG structure, is not so pronounced, showing the strong influence of the limited number of $M \times N$ columns of the investigated lattice with respect to the case of $M = N = \infty$.

We consider now the corresponding active PBG structures: of course the transmittance and reflectance significantly change. Since the spectral characteristics depend on the polarization, throughout all the paper, the results will be illustrated for both TE and TM polarizations. We start our simulations by considering a Lorentzian active material with a spectral gain profile centered in correspondence of the inferior edge of the second photonic band gap, identified by the following parameters: normalized frequency $\omega_n = 0.82$ (corresponding to conductivity peak wavelength value $\lambda_0 = 1.22\mu$m), $\sigma_0 = -13685\,\mathrm{S/m}$, $T_2 = 0.07\,\mathrm{ps}$. Fig. 16 depicts the TE and TM evaluated transmission and reflection coefficients for the 16×2 active 2D lattice. As expected, the peak value of the transmission coefficient is localized in correspondence of the frequency $\omega_n = 0.82$ that identifies the conductivity maximum value and it reaches the value of about 3.38 for TE polarization and 1.92 for the TM one. These spectra show that the square lattice exhibits better performance for TE polarization. Moreover, it is interesting to outline that even the reflection coefficient spectrum for TE-polarization exhibits a peak just at the normalized frequency value corresponding to the conductivity peak: this occurrence will assume a significant role in the onset of the lasing oscillation.

Let us consider now the effect on the transmission and reflection coefficients of the active period number increasing along the propagation direction, to parity of the other data and, in particular, of conductivity Lorentzian shape. In the case of a 16×4 active lattice, the T peak remarkably increases, reaching the value of about 39 and 4.7 for TE and TM polarization, respectively. The reflection coefficient R for TE polarization increases till to 104 while for TM polarization the R peak is only 0.7. The examined structure gives rise to the stimulated

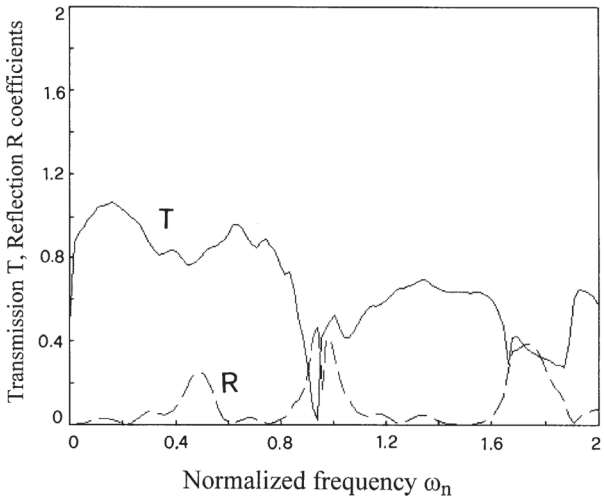

(a)

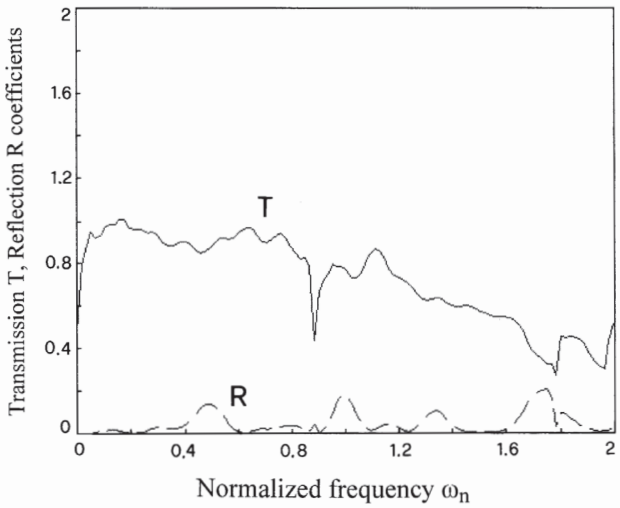

(b)

Figure 15. Transmission and reflection coefficients for the square lattice of 16×2 columns of dielectric passive materials ($\varepsilon_2 = 2.0$) in air: (a) TE polarization, (b) TM polarization.

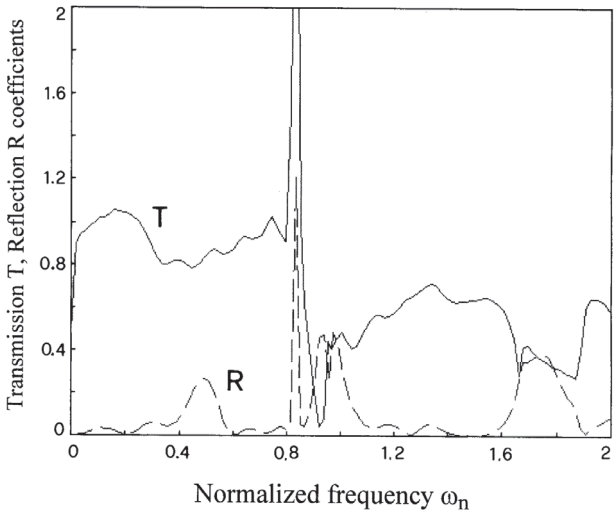

(a)

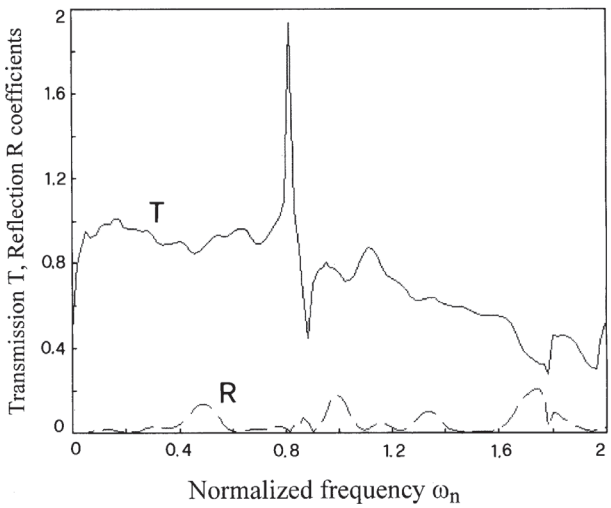

(b)

Figure 16. Transmission and reflection coefficients of the active 16×2 square lattice. The active Lorentzian material is characterized by the following parameters: $\omega_n = 0.82$, $\sigma_0 = -13685\,\mathrm{S/m}$, $T_2 = 0.07\,\mathrm{ps}$: (a) TE polarization, (b) TM polarization.

emission phenomenon as we can infer from Fig. 17 where the time evolution of the electric field component E_y at the output section $z = L$ is depicted: a sinusoidal oscillation just at the frequency $\omega_n = 0.82$, that defines the maximum of the conductivity, is apparent: however its normalized amplitude reaches only the maximum value equal to 0.2. We notice that the field is well confined in the active columns which are denser than the air. This occurrence is more evident in Fig. 17b which shows the magnified plot of the E_y evolution in the output section, restricted to a small range of time steps.

More interesting effects are observable when the number of periods along the z direction is increased. Fig. 18 shows the sum of transmittance and the reflectance for a TE polarized wave propagating in a $16 \times N$ lattice with $N = 2$ (dashed-dotted line), $N = 4$ (dashed line), $N = 8$ (solid line). For $N = 2$ and 4 the sum is equal to about the unity (like for a lossless or a gain less material) in the whole examined spectral large except in correspondence of the inferior edge of the band gap where we superimposed the conductivity peak and a large enhancement, due to the stimulated emission, is apparent. By further increasing the number of the active lattice periods to $N = 8$ the sum of transmittance and reflectance assumes a value equal to 30 dB in a small range of low normalized frequencies near the origin, it settles in a value a bit lower than 10^3 dB in the whole spectral range and the peak at the band edge reaches a noticeable large value, the enhancement factor being four orders of magnitude greater. This effect seems to be a phenomenon of saturation due to the high value of the assumed conductivity peak. In fact, in this case the transmission and reflection spectra do not exhibit the usual band structure and, therefore, the periodic lattice behaves as a bulk active medium. In the case of TM polarization, the sum of transmittance and reflectance exhibits a more regular shape well settled equal to unit in the whole spectral range with the peak fixed in correspondence of the conductivity peak, for all the considered N values. The peak value, obtained for the $N = 8$ period lattice along the z direction reaches 200 dB. The effect of saturation for this type of polarization does not turn up.

Fig. 19 illustrates the time evolution of the TE-polarized field component E_y at the output section $z = L$ of the 16×8 square lattice and other data as those in Fig. 16. By increasing the number of the active layers along the propagation direction, the normalized amplitude of the field component increases being two order of magnitude greater than the field amplitude evaluated for the 16×4 lattice. Moreover, a lasing oscillation is established just at the frequency that defines the maximum of the conductivity. The maximum amplitude of oscillation is localized in correspondence of the central section along the x-axis.

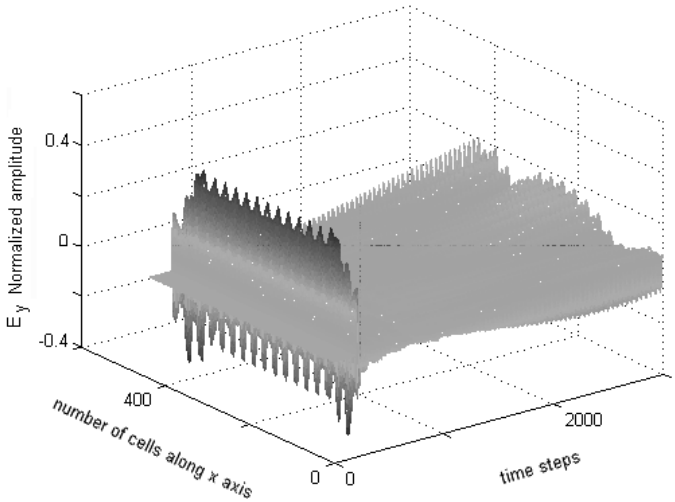

(a)

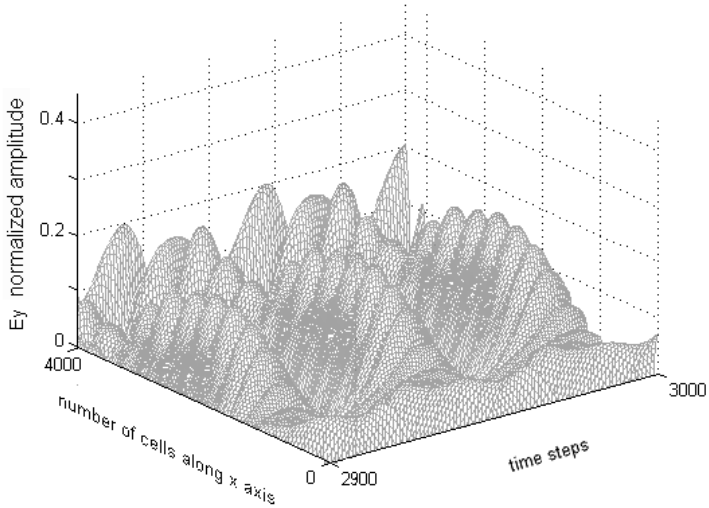

(b)

Figure 17. Time evolution of the electric field component E_y at the output section of 16×4 active square lattice; (b) expanded time scale of the steady-state region showing a single mode oscillation at λ_0. Other data as those in Fig. 16.

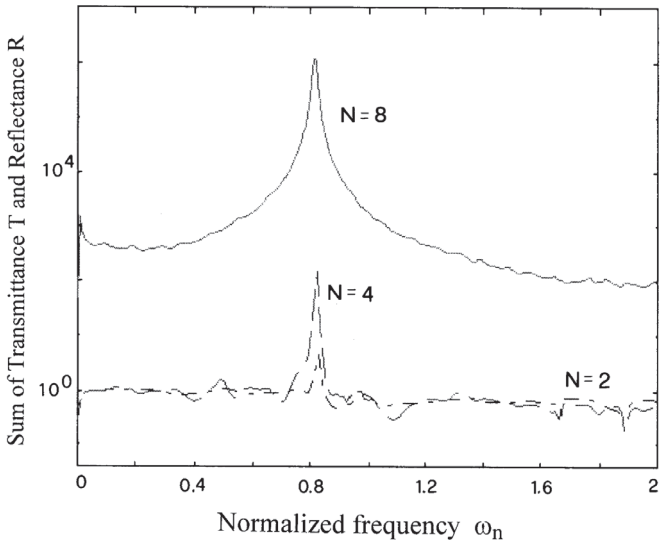

Figure 18. Sum of transmittance and reflectance for a TE polarized wave propagating in a $16 \times N$ square lattice: $N = 2$ (dashed-dotted line), $N = 4$ (dashed line), $N = 8$ (solid line).

Another parameter that influences the characteristics of the PBG structure is the lattice shape. We now investigate the passive photonic crystal having a chess-board lattice (see Fig. 16b) characterized by the presence of a dielectric active column in the center of the cross section of the square elementary cell. The band structure of the infinite passive PhC, with respect to the square lattice, is characterized by the absence of the band gap localized in correspondence of the normalized frequency value equal to 0.4 for both polarizations. Moreover the band gap centered at 0.75 is completely open only for the TE polarization.

As for the square lattice, we consider the PGB structure made of an optical gain medium having a Lorentzian spectral gain profile, characterized by the following parameters: $\omega_n = 0.82$ ($\lambda_0 = 1.22\,\mu$m), $\sigma_0 = -13685\,$S/m, $T_2 = 0.07\,$ps. For a 16×2 chess-board lattice, the evaluated transmission peak is 76.43 for TE polarization and 18.98 for TM polarization, much higher than those evaluated for the square lattice: this occurrence is due to the shape of lattice which is characterized by a greater filling factor. In the case of the 16×4 chess-board lattice, the transmittance increases till to 26 dB and 8.6 dB for TE and TM polarizations, respectively.

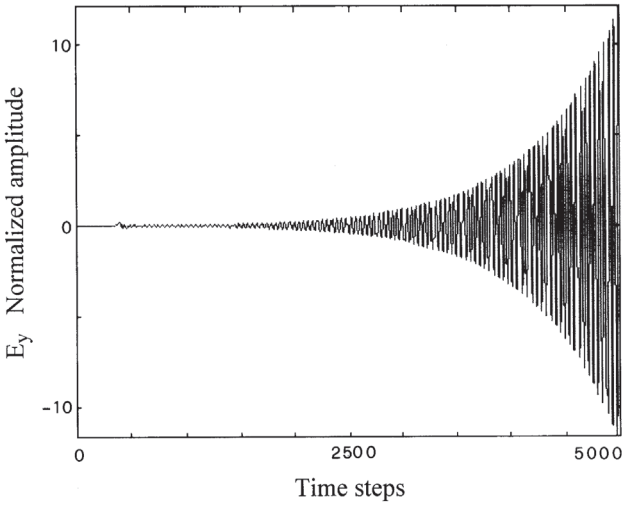

(a)

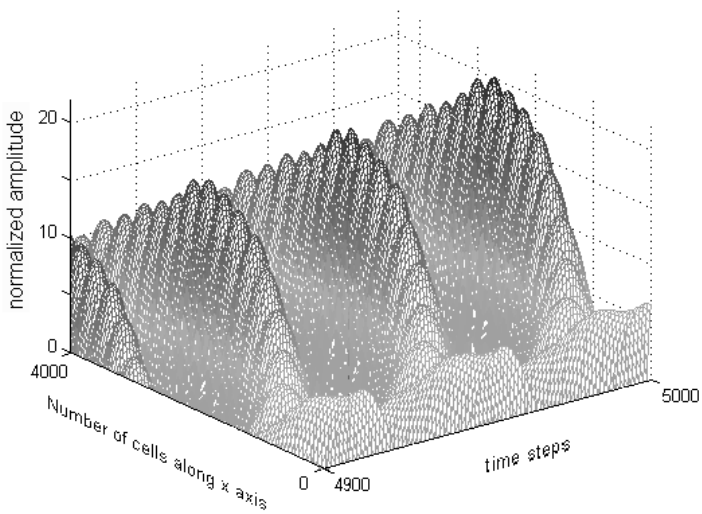

(b)

Figure 19. (a) Time evolution of the electric field component E_y at the output section of the 16×8 period square active lattice; (b) expanded time scale of the steady-state region:a single mode oscillation at λ_0 is apparent.

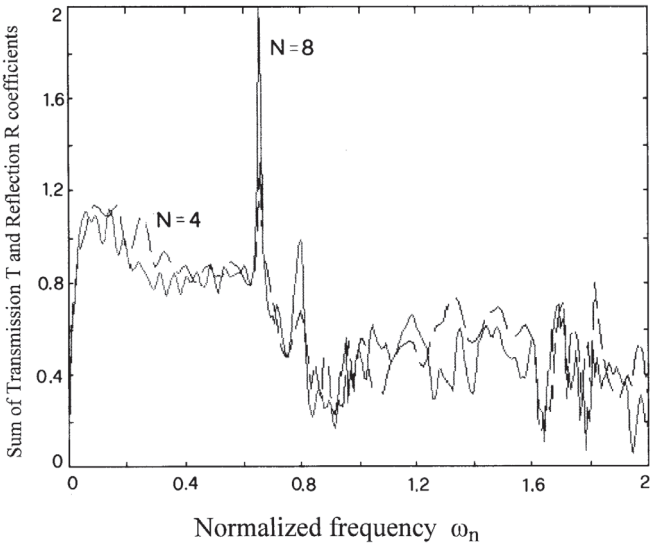

Figure 20. Sum of transmittance and reflectance for a TE polarized wave propagating in a $16 \times N$ chess-board lattice: $N = 4$ (dashed line), $N = 8$ (solid line), being the active Lorentzian material characterized by the following parameters: $\omega_n = 1.22\,\mu$m, $\sigma_0 = -1368\,$S/m, $T_2 = 0.07\,$ps.

Because we obtain substantially high transmission peak values in the structure with a low number of periods along the z direction, and to avoid the saturation effects, we consider a Lorentzian conductivity having the peak value one order of magnitude lower than that assumed for the square lattice, $\sigma_0 = -1368\,$S/m, centered in correspondence of the inferior edge of the first photonic band gap for TE modes. Fig. 20 shows the sum of transmission and reflection coefficients evaluated for the 16×4 and 16×8 chess-board lattices. The peak of $(R+T)$ assumes values equal to 1.3 and 2, respectively. In this case no saturation effect is evident but the evaluated T coefficient values are greater than those evaluated in the case of the square lattice. Of course, the T coefficient values are greater than those evaluated for a 1D structure, to parity of other geometrical and physical parameters, showing the better performance of the 2D active lattice.

To conclude, Tab. 1 shows the evaluated Q-factor, defined as $Q = \omega_c/\Delta\omega$ where ω_c is the resonant angular frequency (in our case, practically equal to ω_0) and $\Delta\omega$ is the full-width at half power of the

Table 1. Q-factor for square and chess-board 2D active lattices consisting of $16 \times N$ rods.

	N=2	N=4	N=8
Square lattice (σ_0=13685 S/m)	TE modes: Q=0.027 TM modes: Q=0.025	TE modes: Q=0.038 TM modes: Q=0.023	TE modes: Q=0.110 TM modes: Q=0.022
Chess-board lattice (σ_0=13685 S/m)	TE modes: Q=0.081 TM modes: Q=0.055	TE modes: Q=0.126 TM modes: Q=0.027	TE modes: Q=1.712 TM modes: Q=0.020

transmitted peak, inherent in two different lattice shapes and crystal sizes. For the square lattice, when the crystal size increases from $N = 2$ to $N = 8$, the Q-factor increases by about an order of magnitude (from 0.027 to 0.110) for TE polarization while for TM polarization it slightly decreases from 0.025 to 0.022. It is interesting to note that the Q-factor for the chess-board lattice, in the same conditions, assumes greater values and already for $N = 4$ the Q-factors for both TE and TM polarizations reach the values obtained for the 16×8 square lattice.

5. CONCLUSION

This paper shows the strength of a proprietary FDTD simulator to model 1D and 2D active photonic crystals. In particular, the effects on the transmission spectrum due to the introduction into the PBG structure of Lorentzian gain materials, have been examined. In the case of 1D active structure an enhancement of the peak value of the transmission coefficient and the onset of lasing in the PBG active stack are obtained by increasing the number of periods of active stack and by setting the maximum value of the conductivity in correspondence of the lower edge of a band gap. Moreover the performance of the active 2D PBG structures depends on the lattice shape and, of course, is better than that of the 1D ones.

APPENDIX A. 2D FDTD ALGORITHM FOR ACTIVE MATERIALS

For self-consistency, we develop here the basic equations of the applied method, devoted to the analysis of two-dimensional structures in presence of active media. The frequency dependent gain is incorporated into the electric current density term in Maxwell's equations by means of a Lorentzian frequency-dependent negative

conductivity. To avoid confusion with respect to other already published papers and books, we exactly follow the notation of Ref. [19] where the guide-lines of the propagation algorithms are discussed.

Two-dimensional ($\partial/\partial y = 0$) Maxwell's equations in rectangular frame coordinates (see Fig. 1), describing the electric and magnetic field components propagating through a nonmagnetic ($\mu = \mu_0$), isotropic medium, are:

$$\begin{aligned}
\frac{\partial H_x}{\partial t} &= \frac{1}{\mu_0}\frac{\partial E_y}{\partial z} \\
\frac{\partial H_y}{\partial t} &= \frac{1}{\mu_0}\left[\frac{\partial E_z}{\partial x} - \frac{\partial E_x}{\partial z}\right] \\
\frac{\partial H_z}{\partial t} &= -\frac{1}{\mu_0}\frac{\partial E_y}{\partial x} \\
\frac{\partial E_x}{\partial t} &= \frac{1}{\varepsilon}\left[-\frac{\partial H_y}{\partial z} - J_x\right] \\
\frac{\partial E_y}{\partial t} &= \frac{1}{\varepsilon}\left[\frac{\partial H_x}{\partial z} - \frac{\partial H_z}{\partial x} - J_y\right] \\
\frac{\partial E_z}{\partial t} &= \frac{1}{\varepsilon}\left[\frac{\partial H_y}{\partial x} - J_z\right]
\end{aligned} \tag{A1}$$

The scalar frequency-dependent conductivity that links the electric field and the current density is given by [19]:

$$\begin{aligned}
\sigma(\omega) &= \frac{J_x(\omega)}{E_x(\omega)} = \frac{J_y(\omega)}{E_y(\omega)} = \frac{J_z(\omega)}{E_z(\omega)} \\
&= \frac{1}{1 + I/I_s}\left(\frac{\sigma_0/2}{1 + j(\omega - \omega_0)T_2} + \frac{\sigma_0/2}{1 + j(\omega + \omega_0)T_2}\right)
\end{aligned} \tag{A2}$$

In this expression the Hermitian symmetry is used for the Lorentzian profile and σ_0 is the peak value of the conductivity, linked to the peak value of the gain set by the pumping level and the resulting population inversion; ω_0 is the frequency pertaining to the peak value of the conductivity; T_2 is a time constant which defines the spreading of the Lorentzian spectral profile, $S = (1 + I/I_s)^{-1}$ is the saturation coefficient while I_s is the saturation intensity. The explicit finite-difference equations for the electric field components are:

$$\begin{aligned}
E_x^{n+1}(i,k) = E_x^n(i,k) &+ \frac{\Delta t}{\varepsilon \Delta z}\left[H_y^{n+1/2}(i,k-1/2) - H_y^{n+1/2}(i,k+1/2)\right] \\
&- \frac{\Delta t}{2\varepsilon}\left[J_x^{n+1}(i,k) + J_x^n(i,k)\right]
\end{aligned} \tag{A3a}$$

$$E_y^{n+1}(i,k) = E_y^n(i,k) + \frac{\Delta t}{\varepsilon \Delta z}\left[H_x^{n+1/2}(i,k+1/2) - H_x^{n+1/2}(i,k-1/2)\right] - \frac{\Delta t}{\varepsilon \Delta x}\left[H_z^{n+1/2}(i+1/2,k) - H_z^{n+1/2}(i-1/2,k)\right] - \frac{\Delta t}{2\varepsilon}\left[J_y^{n+1}(i,k) + J_y^n(i,k)\right] \tag{A3b}$$

$$E_z^{n+1}(i,k) = E_z^n(i,k) + \frac{\Delta t}{\varepsilon \Delta x}\left[H_y^{n+1/2}(i+1/2,k) - H_y^{n+1/2}(i-1/2,k)\right] - \frac{\Delta t}{2\varepsilon}\left[J_z^{n+1}(i,k) + J_z^n(i,k)\right] \tag{A3c}$$

where:

$$J_x^{n+1}(i,k) = J_x^n(i,k) + \frac{\Delta t}{2}\left[F_x^{n+1}(i,k) + F_x^n(i,k)\right]$$
$$J_y^{n+1}(i,k) = J_y^n(i,k) + \frac{\Delta t}{2}\left[F_y^{n+1}(i,k) + F_y^n(i,k)\right]$$
$$J_z^{n+1}(i,k) = J_z^n(i,k) + \frac{\Delta t}{2}\left[F_z^{n+1}(i,k) + F_z^n(i,k)\right]$$

and

$$F_x^{n+1}(i,k) = A_{1x}(i,k)\left[H_y^{n+1/2}(i,k-1/2) - H_y^{n+1/2}(i,k+1/2)\right] + A_{2x}(i,k)E_x^n(i,k) + A_{3x}(i,k)J_x^n(i,k) + A_{4x}(i,k)F_x^n(i,k)$$

$$A_{1x}(i,k) = \frac{4\Delta t S_x(i,k)\sigma_0(\Delta t + 2T_2)}{\beta_x(i,k)\Delta z}$$
$$A_{2x}(i,k) = \frac{8\varepsilon S_x(i,k)\sigma_0 \Delta t}{\beta_x(i,k)}$$
$$A_{3x}(i,k) = -\frac{4\Delta t\left[2\varepsilon\left(1+\omega_0^2T_2^2\right) + S_x(i,k)\sigma_0(\Delta t + 2T_2)\right]}{\beta_x(i,k)}$$
$$A_{4x}(i,k) = -\frac{8\varepsilon T_2(\Delta t - T_2)}{\beta_x(i,k)} - \frac{(\Delta t)^2[2\varepsilon(1+\omega_0^2T_2^2) + S_x(i,k)\sigma_0(\Delta t + 2T_2)]}{\beta_x(i,k)}$$
$$\beta_x(i,k) = 8\varepsilon T_2(\Delta t + T_2) + (\Delta t)^2\left[2\varepsilon\left(1+\omega_0^2T_2^2\right) + S_x(i,k)\sigma_0(\Delta t + 2T_2)\right]$$
$$S_x(i,k) = \left[1 + \frac{I_x(i,k)}{I_s}\right]^{-1}, \qquad I_x(i,k) = 0.5cn\varepsilon_0\left(E_x^{peak}(i,k)\right)^2$$

Here S_x is the saturation coefficient that contains feedback information of the latest peak electric field component E_x. Moreover:

$$
\begin{aligned}
F_y^{n+1}(i,k) = {} & A_{11y}(i,k)\left[H_x^{n+1/2}(i,k+1/2) - H_x^{n+1/2}(i,k-1/2)\right] \\
& + A_{12y}(i,k)\left[H_z^{n+1/2}(i-1/2,k) - H_z^{n+1/2}(i+1/2,k)\right] \\
& + A_{2y}(i,k)E_y^n(i,k) + A_{3y}(i,k)J_y^n(i,k) + A_{4y}(i,k)F_y^n(i,k)
\end{aligned}
$$

where

$$
\begin{aligned}
A_{11y}(i,k) &= \frac{4\Delta t S_y(i,k)\sigma_0(\Delta t + 2T_2)}{\beta_y(i,k)\Delta z} \\
A_{12y}(i,k) &= \frac{4\Delta t S_y(i,k)\sigma_0(\Delta t + 2T_2)}{\beta_y(i,k)\Delta x} \\
A_{2y}(i,k) &= \frac{8\varepsilon S_y(i,k)\sigma_0\Delta t}{\beta_y(i,k)} \\
A_{3y}(i,k) &= -\frac{4\Delta t\left[2\varepsilon\left(1+\omega_0^2T_2^2\right) + S_y(i,k)\sigma_0(\Delta t + 2T_2)\right]}{\beta_y(i,k)} \\
A_{4y}(i,k) &= -\frac{8\varepsilon T_2(\Delta t - T_2)}{\beta_y(i,k)} - \frac{(\Delta t)^2[2\varepsilon(1+\omega_0^2T_2^2) + S_y(i,k)\sigma_0(\Delta t + 2T_2)]}{\beta_y(i,k)} \\
\beta_y(i,k) &= 8\varepsilon T_2(\Delta t + T_2) + (\Delta t)^2\left[2\varepsilon\left(1+\omega_0^2T_2^2\right) + S_y(i,k)\sigma_0(\Delta t + 2T_2)\right] \\
S_y(i,k) &= \left[1 + \frac{I_y(i,k)}{I_s}\right]^{-1}, \qquad I_y(i,k) = 0.5cn\varepsilon_0\left(E_y^{peak}(i,k)\right)^2
\end{aligned}
$$

and

$$
\begin{aligned}
F_z^{n+1} = {} & A_{1z}(i,k)\left[H_y^{n+1/2}(i+1/2,k) - H_y^{n+1/2}(i-1/2,k)\right] \\
& + A_{2z}(i,k)E_z^n(i,k) + A_{3z}(i,k)J_z^n(i,k) + A_{4z}(i,k)F_z^n(i,k)
\end{aligned}
$$

$$
\begin{aligned}
A_{1z}(i,k) &= \frac{4\Delta t S_z(i,k)\sigma_0(\Delta t + 2T_2)}{\beta_z(i,k)\Delta x} \\
A_{2z}(i,k) &= \frac{8\varepsilon S_z(i,k)\sigma_0\Delta t}{\beta_z(i,k)} \\
A_{3z}(i,k) &= -\frac{4\Delta t\left[2\varepsilon\left(1+\omega_0^2T_2^2\right) + S_z(i,k)\sigma_0(\Delta t + 2T_2)\right]}{\beta_z(i,k)} \\
A_{4z}(i,k) &= -\frac{8\varepsilon T_2(\Delta t - T_2)}{\beta_z(i,k)} - \frac{(\Delta t)^2[2\varepsilon(1+\omega_0^2T_2^2) + S_z(i,k)\sigma_0(\Delta t + 2T_2)]}{\beta_z(i,k)} \\
\beta_z(i,k) &= 8\varepsilon T_2(\Delta t + T_2) + (\Delta t)^2\left[2\varepsilon\left(1+\omega_0^2T_2^2\right) + S_z(i,k)\sigma_0(\Delta t + 2T_2)\right] \\
S_z(i,k) &= \left[1 + \frac{I_x(i,k)}{I_s}\right]^{-1}, \qquad I_z(i,k) = 0.5cn\varepsilon_0\left(E_z^{peak}(i,k)\right)^2
\end{aligned}
$$

The explicit update equations for the magnetic field components are:

$$H_x^{n+1/2}(i,k) = H_x^{n-1/2}(i,k) + \frac{\Delta t}{\mu_0}\left[\frac{E_y^n(i,k+1/2) - E_y^n(i,k-1/2)}{\Delta z}\right] \tag{A4a}$$

$$H_y^{n+1/2}(i,k) = H_y^{n-1/2}(i,k) + \frac{\Delta t}{\mu_0}\left[\begin{array}{l}\dfrac{E_z^n(i+1/2,k) - E_z^n(i-1/2,k)}{\Delta x} + \\ -\dfrac{E_x^n(i,k+1/2) - E_x^n(i,k-1/2)}{\Delta z}\end{array}\right] \tag{A4b}$$

$$H_z^{n+1/2}(i,k) = H_z^{n-1/2}(i,k) - \frac{\Delta t}{\mu_0}\left[\frac{E_y^n(i+1/2,k) - E_y^n(i-1/2,k)}{\Delta x}\right] \tag{A4c}$$

Equations (A3)–(A4) constitute the complete FDTD time-stepping algorithm for a Lorentzian dispersive gain medium. This algorithm is second-order accurate in the grid space and time increments, and it reduces to the normal FDTD update equations if $T_2 = 0$.

APPENDIX B. PML TERMINATION FOR CONDUCTIVE DISPERSIVE MEDIA

For simulating Lorentzian optical gain material extending to infinity, the Uniaxial Perfectly Matched Layer (UPML) along a plane boundary has to be matched to the Lorentzian half-space of parameters ε_r and $\sigma(\omega)$.

Hence, Ampere's law in the PML can be expressed as:

$$\begin{bmatrix} \dfrac{\partial}{\partial y}H_z - \dfrac{\partial}{\partial z}H_y \\ \dfrac{\partial}{\partial z}H_x - \dfrac{\partial}{\partial x}H_z \\ \dfrac{\partial}{\partial x}H_y - \dfrac{\partial}{\partial y}H_x \end{bmatrix} = j\omega\varepsilon_0\left(\varepsilon_r + \frac{\sigma(\omega)}{j\omega\varepsilon_0}\right)\begin{bmatrix} \dfrac{s_y s_z}{s_x} & 0 & 0 \\ 0 & \dfrac{s_x s_z}{s_y} & 0 \\ 0 & 0 & \dfrac{s_x s_y}{s_z} \end{bmatrix}\begin{bmatrix} E_x \\ E_y \\ E_z \end{bmatrix} \tag{B1}$$

where s_x, s_y and s_z are [8]:

$$s_i = k_i + \frac{\sigma_i^{PML}}{j\omega\varepsilon_0} \qquad \text{with } i = x, y, z$$

In order to derive a time-dependent representation we introduce some additional auxiliary variables:

$$
\begin{aligned}
&P_x = \frac{s_z}{s_x} E_x, \qquad P_y = \frac{s_x}{s_y} E_y, \qquad P_z = \frac{s_y}{s_z} E_z \\
&P'_x = s_y P_x, \qquad P'_y = s_z P_y, \qquad P'_z = s_x P_z \\
&P''_x = \sigma(\omega) P'_x, \qquad P''_y = \sigma(\omega) P'_y, \qquad P''_z = \sigma(\omega) P'_z
\end{aligned}
$$

Using these expression, Eq. (B1) is decoupled into the set of differential equations:

$$
\begin{bmatrix} \frac{\partial}{\partial y} H_z - \frac{\partial}{\partial z} H_y \\ \frac{\partial}{\partial z} H_x - \frac{\partial}{\partial x} H_z \\ \frac{\partial}{\partial x} H_y - \frac{\partial}{\partial y} H_x \end{bmatrix} = \frac{\partial}{\partial t} \varepsilon_0 \varepsilon_r \begin{bmatrix} P'_x \\ P'_y \\ P'_z \end{bmatrix} + \begin{bmatrix} P''_x \\ P''_y \\ P''_z \end{bmatrix} \tag{B2a}
$$

$$
\left(1 + \omega_0^2 T_2^2 + 2T_2 \frac{\partial}{\partial t} + T_2 \frac{\partial^2}{\partial t^2}\right) \begin{bmatrix} P''_x \\ P''_y \\ P''_z \end{bmatrix} = \left(\sigma_0 + \sigma_0 T_2 \frac{\partial}{\partial t}\right) \begin{bmatrix} P'_x \\ P'_y \\ P'_z \end{bmatrix} \tag{B2b}
$$

$$
\frac{\partial}{\partial t} \begin{bmatrix} P'_x \\ P'_y \\ P'_z \end{bmatrix} = \frac{\partial}{\partial t} \begin{bmatrix} k_y & 0 & 0 \\ 0 & k_z & 0 \\ 0 & 0 & k_x \end{bmatrix} \begin{bmatrix} P_x \\ P_y \\ P_z \end{bmatrix} + \frac{1}{\varepsilon_0} \begin{bmatrix} \sigma_y^{PML} & 0 & 0 \\ 0 & \sigma_z^{PML} & 0 \\ 0 & 0 & \sigma_x^{PML} \end{bmatrix} \begin{bmatrix} P_x \\ P_y \\ P_z \end{bmatrix} \tag{B2c}
$$

$$
\frac{d}{dt}(k_x P_x) + \frac{\sigma_x^{PML}}{\varepsilon_0} P_x = \frac{d}{dt}(k_z E_x) + \frac{\sigma_z^{PML}}{\varepsilon_0} E_x \tag{B2d}
$$

$$
\frac{d}{dt}(k_y P_y) + \frac{\sigma_y^{PML}}{\varepsilon_0} P_y = \frac{d}{dt}(k_x E_y) + \frac{\sigma_x^{PML}}{\varepsilon_0} E_y \tag{B2e}
$$

$$
\frac{d}{dt}(k_z P_z) + \frac{\sigma_z^{PML}}{\varepsilon_0} P_z = \frac{d}{dt}(k_y E_z) + \frac{\sigma_y^{PML}}{\varepsilon_0} E_z \tag{B2f}
$$

These equations are discretized, by applying central-difference approximations to space and time derivatives. The update equations

for the variables P'' are:

$$P_x^{''n+1}(i+1/2,j,k) = C_1 P_x^{''n}(i+1/2,j,k) + C_2 P_x^{''n-1}(i+1/2,j,k) + C_3 P_x^{'n+1}(i+1/2,j,k) + C_4 P_x^{'n}(i+1/2,j,k) \tag{B3a}$$

$$P_y^{''n+1}(i,j+1/2,k) = C_1 P_y^{''n}(i,j+1/2,k) + C_2 P_y^{''n-1}(i,j+1/2,k) + C_3 P_y^{'n+1}(i,j+1/2,k) + C_4 P_y^{'n}(i,j+1/2,k) \tag{B3b}$$

$$P_z^{''n+1}(i,j,k+1/2) = C_1 P_z^{''n}(i,j,k+1/2) + C_2 P_z^{''n-1}(i,j,k+1/2) + C_3 P_z^{'n+1}(i,j,k+1/2) + C_4 P_z^{'n}(i,j,k+1/2) \tag{B3c}$$

where

$$C_1 = -\frac{\left(\dfrac{1+\omega_0^2 T_2^2}{2} - \dfrac{2T_2}{\Delta t} - \dfrac{2T_2}{(\Delta t)^2}\right)}{\left(\dfrac{1+\omega_0^2 T_2^2}{2} + \dfrac{2T_2}{\Delta t} + \dfrac{T_2}{(\Delta t)^2}\right)}$$

$$C_2 = -\frac{\left(\dfrac{T_2}{(\Delta t)^2}\right)}{\left(\dfrac{1+\omega_0^2 T_2^2}{2} + \dfrac{2T_2}{\Delta t} + \dfrac{T_2}{(\Delta t)^2}\right)}$$

$$C_3 = \frac{\left(\dfrac{\sigma_0}{2} + \dfrac{\sigma_0 T_2}{\Delta t}\right)}{\left(\dfrac{1+\omega_0^2 T_2^2}{2} + \dfrac{2T_2}{\Delta t} + \dfrac{T_2}{(\Delta t)^2}\right)}$$

$$C_4 = \frac{\left(\dfrac{\sigma_0}{2} - \dfrac{\sigma_0 T_2}{\Delta t}\right)}{\left(\dfrac{1+\omega_0^2 T_2^2}{2} + \dfrac{2T_2}{\Delta t} + \dfrac{T_2}{(\Delta t)^2}\right)}$$

From (B2a) we obtain the update equations for P'_x, P'_y and P'_z:

$$P_x^{'n+1}(i+1/2,j,k) = \frac{\left[\dfrac{\varepsilon_0\varepsilon_r}{\Delta t} - \dfrac{C_3+C_4}{2}\right]}{\left[\dfrac{\varepsilon_0\varepsilon_r}{\Delta t} + \dfrac{C_3}{2}\right]} P_x^{'n}(i+1/2,j,k) - \frac{\left[\dfrac{C_4}{2}\right]}{\left[\dfrac{\varepsilon_0\varepsilon_r}{\Delta t} + \dfrac{C_3}{2}\right]} P_x^{'n-1}(i+1/2,j,k)$$

$$-\frac{\left[\frac{C_1}{2}\right]}{\left[\frac{\varepsilon_0\varepsilon_r}{\Delta t}+\frac{C_3}{2}\right]}P_x^{''n}(i+1/2,j,k)-\frac{\left[\frac{C_1+C_2}{2}\right]}{\left[\frac{\varepsilon_0\varepsilon_r}{\Delta t}+\frac{C_3}{2}\right]}P_x^{''n-1}(i+1/2,j,k)$$

$$-\frac{\left[\frac{C_2}{2}\right]}{\left[\frac{\varepsilon_0\varepsilon_r}{\Delta t}+\frac{C_3}{2}\right]}P_x^{''n-2}(i+1/2,j,k)+\frac{1}{\left[\frac{\varepsilon_0\varepsilon_r}{\Delta t}+\frac{C_3}{2}\right]}$$

$$\cdot\left\{\begin{array}{l}\left[\frac{H_z^{n+1/2}(i+1/2,j+1/2,k)-H_z^{n+1/2}(i+1/2,j-1/2,k)}{\Delta y}\right]\\ -\left[\frac{H_y^{n+1/2}(i+1/2,j,k+1/2)-H_y^{n+1/2}(i+1/2,j,k-1/2)}{\Delta z}\right]\end{array}\right\}$$

$$P_y^{'n+1}(i,j+1/2,k)=$$

$$\frac{\left[\frac{\varepsilon_0\varepsilon_r}{\Delta t}-\frac{C_3+C_4}{2}\right]}{\left[\frac{\varepsilon_0\varepsilon_r}{\Delta t}+\frac{C_3}{2}\right]}P_y^{'n}(i,j+1/2,k)-\frac{\left[\frac{C_4}{2}\right]}{\left[\frac{\varepsilon_0\varepsilon_r}{\Delta t}+\frac{C_3}{2}\right]}P_y^{'n-1}(i,j+1/2,k)$$

$$-\frac{\left[\frac{C_1}{2}\right]}{\left[\frac{\varepsilon_0\varepsilon_r}{\Delta t}+\frac{C_3}{2}\right]}P_y^{''n}(i,j+1/2,k)-\frac{\left[\frac{C_1+C_2}{2}\right]}{\left[\frac{\varepsilon_0\varepsilon_r}{\Delta t}+\frac{C_3}{2}\right]}P_y^{''n-1}(i,j+1/2,k)$$

$$-\frac{\left[\frac{C_2}{2}\right]}{\left[\frac{\varepsilon_0\varepsilon_r}{\Delta t}+\frac{C_3}{2}\right]}P_y^{''n-2}(i,j+1/2,k)+\frac{1}{\left[\frac{\varepsilon_0\varepsilon_r}{\Delta t}+\frac{C_3}{2}\right]}$$

$$\cdot\left\{\begin{array}{l}\left[\frac{H_x^{n+1/2}(i,j+1/2,k+1/2)-H_x^{n+1/2}(i,j+1/2,k-1/2)}{\Delta z}\right]\\ -\left[\frac{H_z^{n+1/2}(i+1/2,j+1/2,k)-H_z^{n+1/2}(i-1/2,j+1/2,k)}{\Delta x}\right]\end{array}\right\}$$

$$P_z^{'n+1}(i,j,k+1/2)=$$

$$\frac{\left[\frac{\varepsilon_0\varepsilon_r}{\Delta t}-\frac{C_3+C_4}{2}\right]}{\left[\frac{\varepsilon_0\varepsilon_r}{\Delta t}+\frac{C_3}{2}\right]}P_z^{'n}(i,j,k+1/2)-\frac{\left[\frac{C_4}{2}\right]}{\left[\frac{\varepsilon_0\varepsilon_r}{\Delta t}+\frac{C_3}{2}\right]}P_z^{'n-1}(i,j,k+1/2)$$

$$-\frac{\left[\dfrac{C_1}{2}\right]}{\left[\dfrac{\varepsilon_0\varepsilon_r}{\Delta t}+\dfrac{C_3}{2}\right]}P_z^{''n}(i,j,k+1/2)-\frac{\left[\dfrac{C_1+C_2}{2}\right]}{\left[\dfrac{\varepsilon_0\varepsilon_r}{\Delta t}+\dfrac{C_3}{2}\right]}P_z^{''n-1}(i,j,k+1/2)$$

$$-\frac{\left[\dfrac{C_2}{2}\right]}{\left[\dfrac{\varepsilon_0\varepsilon_r}{\Delta t}+\dfrac{C_3}{2}\right]}P_z^{''n-2}(i,j,k+1/2)+\frac{1}{\left[\dfrac{\varepsilon_0\varepsilon_r}{\Delta t}+\dfrac{C_3}{2}\right]}$$

$$\cdot\left\{\begin{array}{l}\left[\dfrac{H_y^{n+1/2}(i+1/2,j,k+1/2)-H_y^{n+1/2}(i-1/2,j,k+1/2)}{\Delta x}\right]\\ -\left[\dfrac{H_x^{n+1/2}(i,j+1/2,k+1/2)-H_x^{n+1/2}(i,j-1/2,k+1/2)}{\Delta y}\right]\end{array}\right\}$$

From (B2c) we obtain the update equations for P_x, P_y and P_z:

$$P_x^{n+1}(i+1/2,j,k)=\frac{\dfrac{k_y}{\Delta t}-\dfrac{\sigma_y^{PML}}{2\varepsilon_0}}{\dfrac{k_y}{\Delta t}+\dfrac{\sigma_y^{PML}}{2\varepsilon_0}}P_x^n(i+1/2,j,k)$$

$$+\frac{1}{\Delta t\left(\dfrac{k_y}{\Delta t}+\dfrac{\sigma_y^{PML}}{2\varepsilon_0}\right)}\cdot\left[P_x^{'n+1}(i+1/2,j,k)-P_x^{'n}(i+1/2,j,k)\right]$$

$$P_y^{n+1}(i,j+1/2,k)=\frac{\dfrac{k_z}{\Delta t}-\dfrac{\sigma_z^{PML}}{2\varepsilon_0}}{\dfrac{k_z}{\Delta t}+\dfrac{\sigma_z^{PML}}{2\varepsilon_0}}P_y^n(i,j+1/2,k)$$

$$+\frac{1}{\Delta t\left(\dfrac{k_z}{\Delta t}+\dfrac{\sigma_z^{PML}}{2\varepsilon_0}\right)}\cdot\left[P_y^{'n+1}(i,j+1/2,k)-P_y^{'n}(i,j+1/2,k)\right]$$

$$P_z^{n+1}(i,j,k+1/2)=\frac{\dfrac{k_x}{\Delta t}-\dfrac{\sigma_x^{PML}}{2\varepsilon_0}}{\dfrac{k_x}{\Delta t}+\dfrac{\sigma_x^{PML}}{2\varepsilon_0}}P_z^n(i,j,k+1/2)$$

$$+\frac{1}{\Delta t\left(\dfrac{k_x}{\Delta t}+\dfrac{\sigma_x^{PML}}{2\varepsilon_0}\right)}\cdot\left[P_z^{'n+1}(i,j,k+1/2)-P_z^{'n}(i,j,k+1/2)\right]$$

From Eqs. (B2d)—(B2f) we obtain the update equations for E_x, E_y, E_z:

$$E_x^{n+1}(i+1/2,j,k) = \frac{\left(\dfrac{k_z}{\Delta t} - \dfrac{\sigma_z^{PML}}{2\varepsilon_0}\right)}{\left(\dfrac{k_z}{\Delta t} + \dfrac{\sigma_z^{PML}}{2\varepsilon_0}\right)} E_x^n(i+1/2,j,k) + \frac{1}{\left(\dfrac{k_z}{\Delta t} + \dfrac{\sigma_z^{PML}}{2\varepsilon_0}\right)}$$
$$\cdot \left\{ \left[\frac{k_x}{\Delta t} + \frac{\sigma_x^{PML}}{2\varepsilon_0}\right] P_x^{n+1}(i+1/2,j,k) - \left[\frac{k_x}{\Delta t} - \frac{\sigma_x^{PML}}{2\varepsilon_0}\right] P_x^n(i+1/2,j,k) \right\} \tag{B4a}$$

$$E_y^{n+1}(i,j+1/2,k) = \frac{\left(\dfrac{k_x}{\Delta t} - \dfrac{\sigma_x^{PML}}{2\varepsilon_0}\right)}{\left(\dfrac{k_x}{\Delta t} + \dfrac{\sigma_x^{PML}}{2\varepsilon_0}\right)} E_y^n(i,j+1/2,k) + \frac{1}{\left(\dfrac{k_x}{\Delta t} + \dfrac{\sigma_x^{PML}}{2\varepsilon_0}\right)}$$
$$\cdot \left\{ \left[\frac{k_y}{\Delta t} + \frac{\sigma_y^{PML}}{2\varepsilon_0}\right] P_y^{n+1}(i,j+1/2,k) - \left[\frac{k_y}{\Delta t} - \frac{\sigma_y^{PML}}{2\varepsilon_0}\right] P_y^n(i,j+1/2,k) \right\} \tag{B4b}$$

$$E_z^{n+1}(i,j,k+1/2) = \frac{\left(\dfrac{k_y}{\Delta t} - \dfrac{\sigma_y^{PML}}{2\varepsilon_0}\right)}{\left(\dfrac{k_y}{\Delta t} + \dfrac{\sigma_y^{PML}}{2\varepsilon_0}\right)} E_y^n(i,j,k+1/2) + \frac{1}{\left(\dfrac{k_y}{\Delta t} + \dfrac{\sigma_y^{PML}}{2\varepsilon_0}\right)}$$
$$\cdot \left\{ \left[\frac{k_z}{\Delta t} + \frac{\sigma_z^{PML}}{2\varepsilon_0}\right] P_z^{n+1}(i,j,k+1/2) - \left[\frac{k_z}{\Delta t} - \frac{\sigma_z^{PML}}{2\varepsilon_0}\right] P_z^n(i,j,k+1/2) \right\} \tag{B4c}$$

Equations (B4) constitute the second-order accurate update for the electric field. The magnetic field update within the PML is identical to that obtained for a non conductive media:

$$H_x^{n+1/2}(i,j+1/2,k+1/2) =$$
$$\frac{\left(k_z - \dfrac{\sigma_z^{PML}\Delta t}{2\varepsilon_0}\right)}{\left(k_z + \dfrac{\sigma_z^{PML}\Delta t}{2\varepsilon_0}\right)} H_x^{n-1/2}(i,j+1/2,k+1/2) + \frac{1}{\mu_0\mu_r\left(k_z + \dfrac{\sigma_z^{PML}\Delta t}{2\varepsilon_0}\right)}$$

$$\cdot\left\{\begin{array}{l}\left[k_x+\dfrac{\sigma_x^{PML}\Delta t}{2\varepsilon_0}\right]B_x^{n+1/2}(i,j+1/2,k+1/2)-\left[k_x-\dfrac{\sigma_x^{PML}\Delta t}{2\varepsilon_0}\right]\\ \cdot B_x^{n-1/2}(i,j+1/2,k+1/2)\end{array}\right\} \tag{B5a}$$

$$H_y^{n+1/2}(i+1/2,j,k+1/2)=$$
$$\frac{\left(k_x-\dfrac{\sigma_x^{PML}\Delta t}{2\varepsilon_0}\right)}{\left(k_x+\dfrac{\sigma_x^{PML}\Delta t}{2\varepsilon_0}\right)}H_y^{n-1/2}(i+1/2,j,k+1/2)+\frac{1}{\mu_0\mu_r\left(k_x+\dfrac{\sigma_x^{PML}\Delta t}{2\varepsilon_0}\right)}$$
$$\cdot\left\{\begin{array}{l}\left[k_y+\dfrac{\sigma_y^{PML}\Delta t}{2\varepsilon_0}\right]B_y^{n+1/2}(i+1/2,j,k+1/2)-\left[k_y-\dfrac{\sigma_y^{PML}\Delta t}{2\varepsilon_0}\right]\\ \cdot B_y^{n-1/2}(i+1/2,j,k+1/2)\end{array}\right\} \tag{B5b}$$

$$H_z^{n+1/2}(i+1/2,j+1/2,k)=$$
$$\frac{\left(k_y-\dfrac{\sigma_y^{PML}\Delta t}{2\varepsilon_0}\right)}{\left(k_y+\dfrac{\sigma_y^{PML}\Delta t}{2\varepsilon_0}\right)}H_z^{n-1/2}(i+1/2,j+1/2,k)+\frac{1}{\mu_0\mu_r\left(k_y+\dfrac{\sigma_y^{PML}\Delta t}{2\varepsilon_0}\right)}$$
$$\cdot\left\{\begin{array}{l}\left[k_z+\dfrac{\sigma_z^{PML}\Delta t}{2\varepsilon_0}\right]B_z^{n+1/2}(i+1/2,j+1/2,k)-\left[k_z-\dfrac{\sigma_z^{PML}\Delta t}{2\varepsilon_0}\right]\\ \cdot B_z^{n-1/2}(i+1/2,j+1/2,k)\end{array}\right\} \tag{B5c}$$

with

$$B_x^{n+1/2}(i,j+1/2,k+1/2)=$$
$$\frac{\left[\dfrac{k_y}{\Delta t}-\dfrac{\sigma_y^{PML}}{2\varepsilon_0}\right]}{\left[\dfrac{k_y}{\Delta t}+\dfrac{\sigma_y^{PML}}{2\varepsilon_0}\right]}B_x^{n-1/2}(i,j+1/2,k+1/2)+\frac{1}{\left[\dfrac{k_y}{\Delta t}+\dfrac{\sigma_y^{PML}}{2\varepsilon_0}\right]}$$

$$\cdot \left\{ \begin{array}{l} \left[\dfrac{E_y^n(i,j+1/2,k+1) - E_y^n(i,j+1/2,k)}{\Delta z} \right] \\ - \left[\dfrac{E_z^n(i,j+1,k+1/2) - E_z^n(i,j,k+1/2)}{\Delta y} \right] \end{array} \right\}$$

$$B_y^{n+1/2}(i+1/2,j,k+1/2) =$$

$$\frac{\left[\dfrac{k_z}{\Delta t} - \dfrac{\sigma_z^{PML}}{2\varepsilon_0} \right]}{\left[\dfrac{k_z}{\Delta t} + \dfrac{\sigma_z^{PML}}{2\varepsilon_0} \right]} B_y^{n-1/2}(i+1/2,j,k+1/2) + \frac{1}{\left[\dfrac{k_z}{\Delta t} + \dfrac{\sigma_z^{PML}}{2\varepsilon_0} \right]}$$

$$\cdot \left\{ \begin{array}{l} \left[\dfrac{E_z^n(i+1,j,k+1/2) - E_z^n(i,j,k+1/2)}{\Delta x} \right] \\ - \left[\dfrac{E_x^n(i+1/2,j,k+1) - E_x^n(i+1/2,j,k)}{\Delta z} \right] \end{array} \right\}$$

$$B_z^{n+1/2}(i+1/2,j+1/2,k) =$$

$$\frac{\left[\dfrac{k_x}{\Delta t} - \dfrac{\sigma_x^{PML}}{2\varepsilon_0} \right]}{\left[\dfrac{k_x}{\Delta t} + \dfrac{\sigma_x^{PML}}{2\varepsilon_0} \right]} B_z^{n-1/2}(i+1/2,j+1/2,k) + \frac{1}{\left[\dfrac{k_x}{\Delta t} + \dfrac{\sigma_x^{PML}}{2\varepsilon_0} \right]}$$

$$\cdot \left\{ \begin{array}{l} \left[\dfrac{E_x^n(i+1/2,j+1,k) - E_x^n(i+1/2,j,k)}{\Delta y} \right] \\ - \left[\dfrac{E_y^n(i+1,j+1/2,k) - E_y^n(i,j+1/2,k)}{\Delta x} \right] \end{array} \right\}$$

REFERENCES

1. Yablonovitch, E., "Inhibited spontaneous emission in solid state physics and electronics," *Phys. Rev. Letters,* Vol. 5D, 2059–2062, 1987.
2. John, S., "Strong localization of photons in certain disordered dielectric superlattices," *Phys. Rev. Letters,* Vol. 58, 2486–2489, 1987.
3. Joannopoulos, J. D., R. D. Meade, and J. N. Winn, *Photonic Crystals. Molding the Flow of Light,* Princeton University Press, 1995.
4. D'Orazio, A., M. De Sario, V. Petruzzelli, and F. Prudenzano,

"Numerical modeling of photonic band gap waveguiding structures," *Recent Research Developments in Optics,* S. G. Pandalai (ed.), 2002.

5. Sakoda, K., "Enhanced light amplification due to group-velocity anomaly peculiar to two- and three-dimensional photonic crystals," *Optics Express,* Vol. 4, No. 5, 167–176, 1999.
6. Dowling, J. P., M. Scalora, M. J. Bloemer, and C. M. Bowden, "The photonic band edge laser: A new approach to gain enhancement," *J. Appl. Phys.,* Vol. 75, 1896–1899, 1994.
7. Ohtaka, K., "Density of states of slab photonic crystals and the laser oscillation in photonic crystals," *Journal of Lightwave Technology,* Vol. 17, No. 11, 2161–2169, November 1999.
8. Vlasov, Yu. A., K. Luterova, I. Pelant, B. Honerlage, and V. N. Astratov, "Enhancement of optical gain semiconductors embedded in three-dimensional photonic crystals," *Appl. Phys. Lett.,* Vol. 71, No. 12, 1616–1618, 1997.
9. Kopp, V. I., B. Fan, H. K. M. Vithana, and A. Z. Genack "Low-threshold lasing at the edge of a photonic stop band in cholesteric liquid crystal," *Opt. Letters,* Vol. 23 No. 21, 1707–1709, 1998.
10. Villeneuve, P. R., S. Fan, and J. D. Joannoupoulos, "Microcavities in photonic crystals: mode symmetry, tunability and coupling efficiency," *Phys. Rev. B,* Vol. 54, 7837–7842, 1996.
11. Kuzmiak, V. and A. A. Maradudin, "Localized defect modes in a two-dimensional triangular photonic crystal," *Phys. Rev. B,* Vol. 57, 15242–15249, 1998.
12. Pottier, P., C. Seassal, X. Letartre, J. L. Leclercq, P. Viktorovitch, D. Cassagne, and J. Jouanin, "Triangular and hexagonal high Q-factor 2-D photonic band gap cavities on III-V suspended membranes," *J. Lightwave Technology,* Vol. 17, 2058–2062, 1999.
13. Qiu, M. and S. He, "Numerical method for computing defect modes in two-dimensional photonic crystals with dielectric or metallic inclusions," *Physics Review B,* Vol. 61, 12871–12876, 2000.
14. Ripin, D. J., K. Y. Lim, G. S. Petrich, P. R. Villeneuve, S. Fan, E. R. Thoen, J. D. Joannopoulos, E. P. Ippen, and L. A. Kolodziejski, "One-dimensional photonic bandgap microcavities for strong optical confinement in GaAs and GaAs/Al_xO_y semiconductor waveguides," *J. Lightwave Technology,* Vol. 17, 2152–2160, 1999.
15. Villeneuve, P. R., S. Fan, and J. D. Joannopoulos, "Microcavities in photonic crystals: Mode symmetry, tunability and coupling

efficiency," *Physics Review B,* Vol. 54, 7837–7842, 1996.

16. Smith, D. R., R. Dalichaouch, N. Kroll, S. Schultz, S. L. McCall, and P. M. Platzman, "Photonic band structure and defects in one and two dimensions," *J. Optical Society of America B,* Vol. 10, 314–321, 1993.
17. Inoue, K., M. Sasada, J. Kawamata, K. Sakoda, and J. W. Haus, "A two-dimensional photonic crystal laser," *Jpn. J. Appl. Phys.,* Vol. 38, Part 2, No. 2B, L157–L159, 1999.
18. Imada, M., S. Noda, A. Chutinan, T. Tokuda, M. Murata, and G. Sasaki, "Coherent two-dimensional lasing action in surface-emitting laser with triangular-lattice photonic crystal structure," *Applied Phys. Letters,* Vol. 75, No. 3, 316–318, 1999.
19. Taflove, A., *Advances in Computational Electrodynamics — The Finite-Difference Time-Domain Method,* Artech House, 1998.
20. Yariv, A., *Quantum Electronics,* Wiley, New York, 1967.
21. Nojima, S., "Enhancement of optical gain in two-dimensional photonic crystals with active lattice points," *Jpn. J. Applied Physics 2, Lett.,* Vol. 37, L565–L567, 1998.
22. Bell, P. M., J. B. Pendry, L. Martin Moreno, and A. J. Ward, *Comput. Phys. Commun.,* Vol. 85, 306, 1995.